On the unsteady aerodynamics of a surging airfoil at 90◦ incidence

Xu, Guanqun; Sciacchitano, Andrea; Ferreira, Carlos; Yu, Wei

DOI
10.1007/s00348-025-04011-2

Publication date
2025

Document Version
Final published version

Published in
Experiments in Fluids

Citation (APA)
Xu, G., Sciacchitano, A., Ferreira, C., & Yu, W. (2025). On the unsteady aerodynamics of a surging airfoil at 90◦ incidence. *Experiments in Fluids*, *66*(5), Article 85. https://doi.org/10.1007/s00348-025-04011-2

Experiments in Fluids (2025) 66:85
https://doi.org/10.1007/s00348-025-04011-2

RESEARCH ARTICLE

On the unsteady aerodynamics of a surging airfoil at 90° incidence

Guanqun Xu[1] · Andrea Sciacchitano[1] · Carlos Ferreira[1] · Wei Yu[1]

Received: 5 December 2024 / Revised: 25 February 2025 / Accepted: 2 March 2025

Abstract

Wind turbine blades in standstill or parked conditions often experience large angles of attack (AoA), where vortex-induced vibrations (VIV) may occur that increase the risk of structural damage. To better understand the VIV of airfoils at high AoA from an aerodynamic perspective, we conducted experimental investigations into the vortex dynamics of a surging airfoil at a 90° incidence undergoing forced vibrations. Experiments were conducted at two reduced frequencies (k) to demonstrate the lock-in effect, where the vortex shedding frequency aligns with the motion frequency. Results indicate distinct vortex shedding behaviors: at higher k value of 0.38, downstream wake vortices form when the airfoil is moving upwind, while upstream vortices emerge during the downwind motion, interacting with the downstream vortices and leading to an outward flow. At lower k value of 0.19, the wake remains directed to the downwind side, regardless of the airfoil's motion direction. Lock-in is evident in both cases, with one vortex pair shed per cycle at lower k and two pairs at higher k. Furthermore, the study examines the influence of vortex dynamics on unsteady aerodynamic loads. The results show that drag peaks when the airfoil moves upwind near the center position of its trajectory; at higher k, negative drag occurs as the airfoil moves downwind near the center, driven by the interactions among convection, turbulent momentum, pressure, and viscous forces. A reduced-order load estimation model for a flat plate is applied to the experimental data, showing good agreement during the upwind motion of the airfoil, which is the design condition for the original flat plate model. However, during the downwind motion, as the flow condition does not match the original flat plate design condition, the circulatory part of the model is modified to account for the presence of two pairs of vortices in the flow field, yielding improved agreement with the drag values determined from the measured flow field. The findings highlight distinct flow patterns and vortex interactions for the two motion cases, offering insights into their impact on aerodynamic loads.

1 Introduction

Wind energy plays a vital role in fulfilling the worldwide increasing need for renewable energy. In the last ten years (2013–2023), the worldwide installed wind power capacity has increased by three times (Statista 2024). However, during certain incoming wind conditions of wind shear events, extreme wind speed and rapid change in wind speed and direction (IEC 2005), the wind turbine needs to remain idle or even parked to maintain its integrity. When a wind turbine is parked, the pitch angle of the blade is much higher than in normal operating conditions; for example, the SCADA data shows a pitch angle of 78° or 88.3° for the standstill/parked wind turbine in the Belwind wind farm in the north sea (Shirzadeh et al. 2015). In this case, the slender wind turbine blades might experience vortex-induced vibrations (VIV), increasing the blade fatigue loads and leading to structural damage. VIV happens when the vortex shedding frequency synchronizes with the structural frequency, resulting in large structural displacements and structural loads (Williamson and Govardhan 2004). Such a phenomenon occurs in many engineering situations, such as bridges, offshore structures, transmission lines, etc. In the past few decades, much research has been conducted on this topic, as demonstrated by the reviews from Bearman (1984), Williamson and Roshko (1988), and Sarpkaya (2004). A relevant phenomenon occurring in Vortex Induced Vibrations is the so-called lock-in effect. In Bearman's review (1984), the lock-in region, also called the "range of capture," refers to a narrow range of reduced velocities- defined as the ratio of the free-stream velocity to the product of the bluff body's characteristic dimension and its oscillation frequency- where the flow

✉ Guanqun Xu
G.Xu-1@tudelft.nl

[1] Department of flow physics and technology, Delft University of Technology, Kluyverweg 1, 2629 HS Delft, South-Holland, Netherlands

Published online: 07 April 2025

conditions around the bluff body, as well as the force coefficient, change rapidly. Williamson and Roshko (1988) define the lock-in as the condition where the structural oscillation frequency and the vortex formation frequency are close to the structure's natural frequency. The authors also point out that large amplitude motion can be triggered at frequencies that are hundreds of times larger than the structural natural frequency. This is confirmed in the work of Sarpkaya, who showed that lock-in can happen at the super-harmonics of the natural frequency (Sarpkaya 2004).

Although much research has been conducted on VIV, it mainly focuses on cylindrical structures, which are representative of many engineering setups. Instead, limited research can be found on airfoil VIV, a topic that has recently become more relevant owing to the increasing size of wind turbines. Most of the latter research uses numerical simulations; the most pertinent works are presented here. Heinz et al. (2016) studied the aero-elastic response of a DTU 10MW wind turbine blade; their results suggest that with a certain combination of wind speed and incidence, the blade tip vibration can reach several chord lengths. Skrzypiński et al. (2013) numerically investigated the VIV on an airfoil at 90° AoA. The forced vibration (in the chordwise direction) case showed that negative aerodynamic damping happened for oscillation frequencies near the static vortex shedding frequency. A recent research from Pirrung et al. (2024) conducted a full turbine-level simulation in a fluid–structure interaction setup to study the effect of VIV. The results showed that VIV induces both edgewise and flapwise motions onto the three blades, whose amplitude depends on the incoming wind condition and turbine setup. As these results focused on the whole blade and wind turbine level, the detailed flow structures around the blades were not investigated, thus leaving open questions about the physics behind lock-in.

Sarpkaya (2004) also pointed out that, during the free vibration motion, the frequency of object oscillation and vortex shedding at lock-in cannot remain constant over time due to the continuous change of added mass. Instead, the problem has often been addressed by considering forced vibration conditions, whereby the frequency and amplitude of the object's motion can be maintained constant. It is important to note that under the forced vibration condition, the classical definition of lock-in needs to be modified. For the forced oscillation of a circular cylinder, Bishop and Hassan (1964) define lock-in/synchronization when the forcing frequency (f) approaches the vortex shedding frequency (f_{st}). This is the definition used in this research, which is also used in Besem et al. (2016) and Tang and Dowell (2014).

Since the pioneering research into establishing inviscid models for unsteady airfoils from Theodorsen (1935), Sears Sears (1938) and Mayo Greenberg (1947), several related works have been performed over the past decades. The following discussions highlight the most relevant topics related to vortex dynamics, the lock-in effect, and aerodynamic loads for an airfoil setup.

Young and Lai (2004) studied the wake structures of a plunging airfoil by varying the motion's oscillation frequency and amplitude. The results showed that the leading edge separation is the dominant effect in the aerodynamic force until a specific reduced frequency (k). Detailing the wake structures revealed that the reduced frequency k has a significant role in the vortex shedding frequency. The plunging and surging airfoil was studied by Choi et al. (2013), who found out that, for different motion amplitudes, there exist two separate ranges of k values where the lift force generated by the moving airfoil is maximized and minimized, respectively. However, this result only considers the cycle-averaged force, whereas the evolution of the loads along a cycle and the associated vortices were not investigated. By studying the wake structure, Young and Lai (2007) classified the wake shedding modes of the plunging airfoil, and defined an asymmetric lock-in boundary about the natural shedding frequency. The authors attributed this asymmetry to the sharp trailing edge of the airfoil that forces the vortex to shed from the windward side of the airfoil for most of the plunging cycle. Even though these results provide valuable insights into vortex dynamics and frequency lock-in on the airfoil, they focus on a limited range of low angles of attack (typically below 15°). In contrast, the unsteady aerodynamics of airfoils at high angles of attack (AoA) have not been investigated.

The present work is motivated by the need for additional insight into the VIV of airfoils at high AoA from an aerodynamic perspective. Following the same approach as Young and Lai (2004) and Choi et al. (2013) which investigate forced vibrations on airfoils, the case of an airfoil undergoing forced surging motion is considered. The main goal is to investigate the vortex structures from formation, evolution to shedding and their role in the aerodynamic forces. In the following sections, the experimental approach and analysis methodology are introduced. Then, an overview of vortex kinematics and flow development is provided for the two motion cases at each phase of the measurement. The main results detailing the aerodynamic forces are discussed in two sections: (i) the overall force and the contribution of each force component and (ii) the comparison of the experimental data with the flat plate reduced-order model.

2 Methodology

2.1 Experimental setup

2.1.1 Wind tunnel setup

The experiments were conducted in the open jet facility (OJF) of Delft University of Technology. The OJF is a closed-circuit wind tunnel with an open, $2.85 \times 2.85m$ octagonal test section. The setup is depicted in Fig. 1 and is described in detail in Xu et al. (2024).

2.1.2 Wing model

A 40 cm span wing with NACA0021 airfoil of 7.5 cm chord was used in the experimental campaign. The model was 3D printed, and carbon fiber strips were attached at the location of the one-quarter chord to enhance its stiffness. The AoA of the wing was fixed at 90°. A motor with a slider-crank mechanism was used for the surging motion of the wing. The wing is subjected to the sinusoidal surging motion (i.e., parallel to the free-stream direction), with a nominal amplitude of $1.1c$, similar to the simulation from Heinz et al. (2016). The motion frequency was set to 5 Hz and 2.5 Hz, yielding the reduced frequencies ($k = \pi fc/U_\infty$) of 0.38 and 0.19, respectively. In order to trigger lock-in phenomenon, an appropriate combination of motion frequency and amplitude needs to be considered. As was discussed by Koopmann (1967), Anagnostopoulos (2000), and Meneghini and Bearman (1995), the boundary of the lock-in region presents a V-shape: the larger the departure of the frequency ratio f/f_{st} from unity, being f_{st} the static vortex shedding frequency, the larger the amplitude required to trigger lock-in. Considering that the static vortex shedding frequency was $f_{st} = 6.4$ Hz (the procedure to obtain the static shedding frequency is discussed in the results section), and the limitations of the motor, at the highest motion frequency of 5 Hz, the frequency ratio was $f/f_{st} = 0.78$, corresponding to a reduced frequency $k = 0.38$. The motion frequency 2.5 Hz was also investigated in the experiments, yielding $f/f_{st} = 0.39$ and $k = 0.19$. The experimental parameters are summarized in Table1 (Xu et al. 2024). The wing's kinematic motion is driven by a slider-crank linkage, which transfers a circular motion to a linear motion. The wing's actual motion amplitude h is obtained by physically tracking the airfoil leading edge position from the phase-averaged particle image velocimetry (PIV) images. The velocity $\dot{h}$ and acceleration $\ddot{h}$ of the motion were calculated by temporal derivatives of the wing's positions. The results of the wings kinematics are shown in Fig. 2a, and the relative locations are shown in Fig. 2b for four phases of the motion: 0° and 180°, corresponding to the wing's position close to the center of its trajectory, 90° and 270°, corresponding to the most upwind and downwind positions, respectively.

2.1.3 PIV measurements

Stereoscopic PIV measurements were performed to evaluate the flow fields surrounding the wing. A SAFEX smoke generator created water-glycol droplets with a median diameter of 1 μm to seed the flow within the tunnel. The illumination was provided by a Quantel Evergreen Nd:YAG laser (200mJ pulse energy, maximum 15Hz repetition rate, 532nm wavelength). To acquire the three velocity components within the measurement domain, two

Table 1 Experimental parameters

Parameter	Symbol	Value
Freestream velocity	U_∞	3.1m/s
Model chord	c	0.075m
Reynolds number	Re	1.5×10^4
Static vortex shedding frequency	f_{st}	6.4 Hz
Model angle of attack	AoA	90°
Model span	s	0.4m
Model aspect ratio	AR	5.33
Motion frequency	f	2.5Hz, 5Hz
Reduced frequency	k	0.19, 0.38
Frequency ratio	f/f_{st}	0.39, 0.78
Motion amplitude	h_{max}	0.083m($1.1c$)

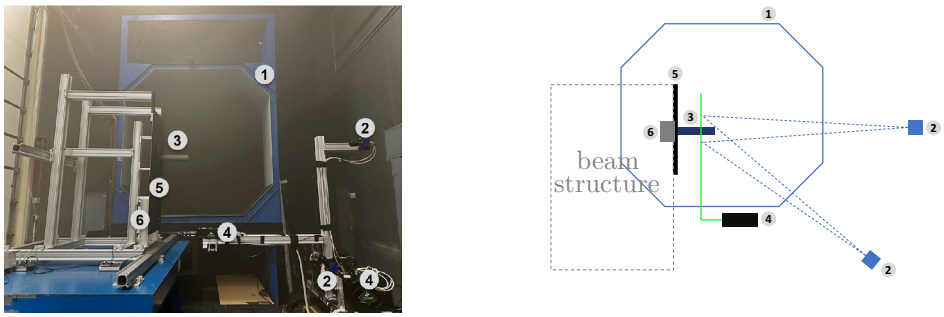

Fig. 1 Experimental setup of the experiments in the OJF, looking in the upstream direction. The relevant components are: 1. Flow outlet 2. LaVision Imager sCMOS camera 3.Airfoil model 4. Quantel Evergreen Nd:YAG laser 5. The base plate 6. Surging mechanism. Note that the schematic plot of the experimental setup (on the right) is not to scale

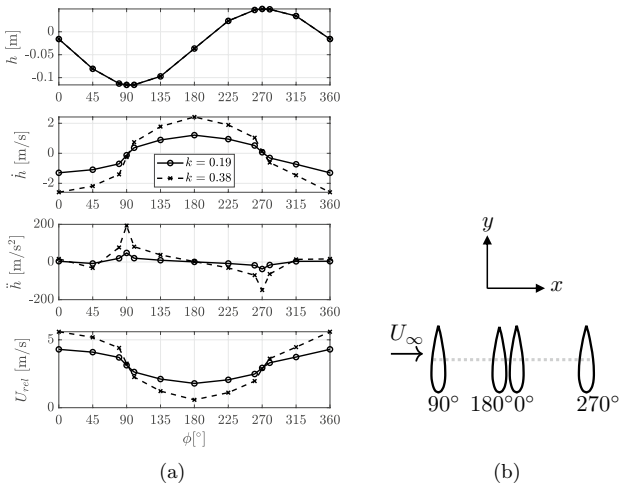

Fig. 2 **a** The actual motion amplitude (h) based on the leading edge of the airfoil, velocity ($\dot{h}$) and acceleration ($\ddot{h}$) of the surging motion for two motion frequencies. Note that the lines for h overlap each other since two cases have the same travel distance. The bottom panel represents the relative wind speed ($U_{\text{rel}} = U_\infty - \dot{h}$) experienced by the airfoil. **b** The relative locations of the airfoil at four different phases: 0° and 180° where the wing is near the center of its trajectory, 90° and 270°, where it is in the most upwind and downwind positions, respectively

LaViSion Imager sCMOS cameras (2560 × 2160 pixel, 16 bit, 6.5 × 6.5 μm pixel size) were installed at the tunnel's side at a relative angle of 40°, as shown in Fig. 1. The size of a single field of view (FoV) is 269.4 × 331.8 mm, which corresponds to approximately 3.6c in the streamwise direction and 4.4c in the cross-flow direction. The image magnification factor is 0.05 with a digital resolution of 7.92 pixels/mm. The experimental procedure involved two stages: initially, a measurement with the static wing was performed to determine the static vortex shedding frequency f_{st}, which was then used to select the frequencies for unsteady measurements. Two single FoVs were stitched together, giving the total FoV of 5.2c in the streamwise direction and 4.2c in the cross-flow direction. Secondly, the unsteady measurements were performed for the surging airfoil. The measurement plane was placed at a distance of 3c from the tip of the wing where the flow is less affected by the three-dimensional effects occurring at the wing tip. To achieve a broader FoV, the entire PIV system was traversed twice in the streamwise direction, which gives the total FoV of 8c in the streamwise direction and 4.2c in the cross-flow direction. Phase-averaged acquisitions were obtained at 12 phases: 0°, 45°, 80°, 90°, 100°, 135°, 180°, 225°, 260°, 270°, 280°, and 315°. For each phase at each local FoV, 200 image pairs were captured, and the time interval between the images of a pair is 120 ms.

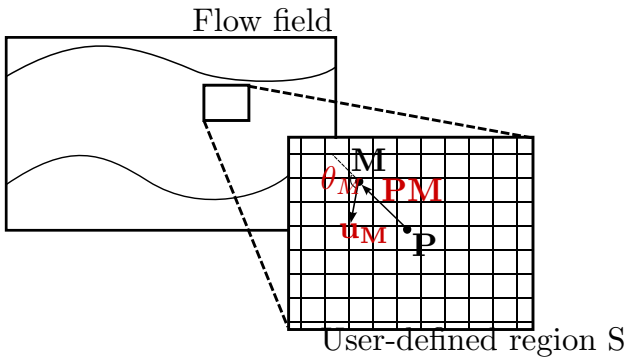

3 Illustration of Γ_1 method

2.1.4 Uncertainty analysis of the PIV measurements

The uncertainty of the PIV measurements can be estimated from the ensemble data size and the flow velocity fluctuation (Ye et al. 2016). For each phase measured, 200 uncorrelated snapshots were taken; hence, the standard uncertainty of the phase-average flow velocity is equal to:

$$\varepsilon_u = \frac{\sigma_u}{U_\infty \sqrt{N}} \tag{1}$$

σ_u is the representative standard deviation value of the streamwise velocity component (σ_u/U_∞ is approximately 0.1 in the wake of the wing) and N represents the number of uncorrelated samples. This equation yields $\varepsilon_u \approx 0.7\%$ for the present experiment.

The uncertainty of the root mean square (RMS) of the velocity fluctuations is estimated as (Sciacchitano and Wieneke 2016):

$$\varepsilon_{u'} = \frac{\sigma_u}{U_\infty \sqrt{2(N-1)}} \tag{2}$$

The expression yields $\varepsilon_{u'} \approx 0.5\%$.

2.2 Vortex identification method and calculation of circulation

Following the approach from Laurent Graftieaux et al. (2001) and Morgan et al. (2009), the so-called Γ_1 method is introduced here, which is employed to identify the vortex center(s) in the flow field.

The illustration of the method is shown in Fig. 3. Given a two-dimensional flow field as those measured by PIV, a user-defined rectangular region S is selected, composed of N data points. Let P be a fixed center point in this region. At each point M within the region S, θ_M is the angle between the location vector **PM** and the velocity vector

$\mathbf{u_M}$. The sine of the angle θ_M can then be calculated, which gives the dimensionless scalar function Γ_1 at P:

$$\Gamma_1(P) = \frac{1}{N}\sum_S \frac{\mathbf{PM}\times\mathbf{u}_\mathrm{M}}{\|\mathbf{PM}\|\cdot\|\mathbf{u}_\mathrm{M}\|} = \frac{1}{N}\sum_S \sin(\theta_M) \tag{3}$$

The value of Γ_1 is calculated for all the data points in the measurement domain. Notice that $|\Gamma_1|$ is bounded by 1; such bound is reached at the center of the vortex if the vortex is axisymmetric. Typically, $|\Gamma_1|$ near the vortex center is between 0.9 and 1.

Once the center of the vortex has been identified using the Γ_1 criterion, the circulation Γ of the vortex can be computed by integration of the vorticity ω within a certain area A:

$$\Gamma = \iint_A \omega\, dA \tag{4}$$

The area A can be selected based on the vortex boundary, identified using the Γ_2 method (Laurent Graftieaux et al. 2001; Morgan et al. 2009). However, in the present work, because the vortices are shed from the leading and trailing edges and separated, a user-defined area is selected as follows. For each phase of measurement, a rectangle boundary is set around each vortex in the flow field; the region is large enough to cover more than the area of the vortex. Then, the integration for the circulation using Eq. 4 is performed, excluding the contribution from the vortices in the opposite direction (opposite sign of vorticity). The schematic plot is shown in Fig. 4.

2.3 Load estimation method

Due to the highly unsteady character of the flow, unsteady load measurements are difficult to conduct with conventional load cells. However, from the PIV velocity data, the derivative-moment transformation method (Rival and Oudheusden 2017) can be used to infer the aerodynamic loads for incompressible unsteady flows. The method is explained below.

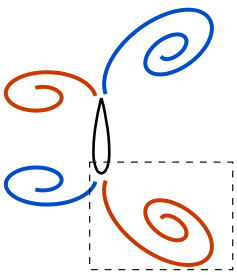

Fig. 4 Demonstration of the user-defined area for circulation calculation. The dashed rectangle represents the user-defined area. The red and blue curls represent the vortices with opposite signs

First, the pressure gradient can be obtained through the Reynolds Averaged Navier–Stokes equation:

$$-\frac{1}{\rho}\frac{\partial(\overline{p})}{\partial x_i} = \frac{\partial(\overline{u}_i)}{\partial t} + \overline{u}_j\frac{\partial(\overline{u}_i)}{\partial x_j} - \nu\frac{\partial^2(\overline{u}_i)}{\partial x_j\partial x_j} + \frac{\partial(\overline{u_i'u_j'})}{\partial x_j} \tag{5}$$

where $\overline{u}_i$ represents the time-average velocity component for the static case (and phase-average for the surging case) in the i direction, $\overline{p}$ is the time-average pressure for the static case (and phase-average for the surging case), ν is the kinematic viscosity, ρ is the air density and $\overline{u_i'u_j'}$ represents the Reynolds stress tensor. The pressure $\overline{p}$ can then be calculated by reformulating the problem as the Poisson equation for pressure, as described by Van Oudheusden (2013), with appropriate boundary conditions: for the inlet of undisturbed flow, the Dirichlet boundary condition is applied; for the remaining boundaries, Neumann boundary conditions are applied.

Second, for two-dimensional evaluation, the aerodynamic forces can be evaluated via the conservation of momentum in a control contour around the airfoil body (Rival and Oudheusden 2017), following the approach employed by Ragni et al. (2011) and Van De Meerendonk et al. (2016) for load evaluations from phase-locked PIV measurements:

$$\bar{F}_i = -\rho\frac{\partial}{\partial t}\iint_l (x_i\bar{u}_i n_i)dl^2 - \rho\iint_l \bar{u}_i\bar{u}_j n_j dl^2 - \rho\iint_l \overline{u_i'u_j'}n_j dl^2 - \iint_l \bar{p}n_i dl^2 + \rho\nu\iint_l \left(\frac{\partial\bar{u}_i}{\partial\bar{x}_j} + \frac{\partial\bar{u}_j}{\partial\bar{x}_i}\right)n_j dl^2 \tag{6}$$

with l the control contour and n_i, n_j the normal unit vector (pointing outward) in the i and j directions, respectively. From left to right of the right-hand side of the equation, the integrals represent the contributions to the aerodynamic loads from the flow unsteadiness, mean convection, turbulence momentum transfer, pressure and mean viscous stress. Note that in the present approach of phased-locked PIV measurements, the FoV is fixed for different phases. Thus, the flow unsteadiness term (the first term on the right-hand side) in Eq. 6 can be written as:

$$-\rho\frac{\partial}{\partial t}\iint_l (x_i\bar{u}_i n_i)dl^2 = -\rho\iint_l \left(x_i\frac{\partial\bar{u}_i}{\partial t}n_i\right)dl^2 \tag{7}$$

Specifically, $\frac{\partial\bar{u}_i}{\partial t}$ is obtained from the consecutive phases measured, as shown in Eq. 8:

$$\frac{\partial\bar{u}_i}{\partial t} = \frac{\partial\bar{u}_i}{\partial\phi_k}\frac{\partial\phi_k}{\partial t} = \frac{\partial\bar{u}_i}{\partial\phi_k}2\pi f \approx \frac{\bar{u}_{i,k+1}-\bar{u}_{i,k-1}}{\phi_{k+1}-\phi_{k-1}}2\pi f \tag{8}$$

Here, ϕ_k denotes the phase at the k-th point in the cycle and $\phi_k = 2\pi ft$. $\bar{u}_{i,k+1}$ and $\bar{u}_{i,k-1}$ are the phase-averaged velocities at the adjacent phases.

Equation 6 is valid when the flow is incompressible and the body is thin (Rival and Oudheusden 2017). In this work, the airfoil NACA 0021 at 90° AoA acts as a bluff body, thus yielding an additional body force term on the right side of Eq. 6:

$$F(t)_B = -\rho B \frac{\partial \dot{h}}{\partial t} \tag{9}$$

where B is the surface area of the airfoil's cross section and $\frac{\partial \dot{h}}{\partial t}$ is the airfoil's acceleration.

2.4 Analytical solution for the surging airfoil

2.4.1 Accelerating motion in one direction

Since the surging airfoil has a fixed AoA of 90°, its shape and the resulting flow dynamics resemble that of a flat plate normal to the free-stream direction, whereby the leading and trailing edge vortices are dominant. This research compares a low-order model of a flat plate at 90° incidence presented by Corkery et al. (2017) with the loads estimated from PIV. In the low-order model, the vortices are assumed to be concentrated into two parts: a leading edge vortex (LEV) and a trailing edge vortex (TEV). The analytical solution for the accelerating flat plate is presented below.

This method decomposes the force into the added mass force (non-circulatory force) and the circulatory force. The former is due to the acceleration induced by the plate to the flow and is equal to the product between added mass and acceleration:

$$F_{\text{non-circ}} = \frac{\rho \pi c^2}{4} \ddot{h} \tag{10}$$

This force can be non-dimensionalized with respect to the dynamic pressure force $(1/2\rho c U_\infty^2)$ to obtain the force coefficient:

$$C_{\text{non-circ}} = \frac{\pi c}{2U_\infty^2} \ddot{h} \tag{11}$$

The circulatory force, instead, is ascribed to the vortex pair generated by the impulsive motion of the plate. If the strengths of the two vortices are $\pm\Gamma$, with the distance d between the cores of the two, the impulse (momentum) (Lamb 1945) of the vortex pair is:

$$J = \rho \Gamma d \tag{12}$$

The time derivative of Eq. 12 gives the force in the streamwise direction:

$$F_{\text{circ}} = \rho(\dot{\Gamma} d + \Gamma \dot{d}) \tag{13}$$

where $\dot{\Gamma}$ and $\dot{d}$ are the time derivative of circulation and vortex distance, respectively. The schematic plot of the model is shown in Fig. 5.

The circulatory force can then be non-dimensionalized with respect to dynamic pressure force $(1/2\rho c U_\infty^2)$ as:

$$C_{\text{circ}} = \frac{2}{U_\infty^2 c}(\dot{\Gamma} d + \Gamma \dot{d}) \tag{14}$$

The total drag force coefficient C_d is the sum of the non-circulatory and circulatory terms:

$$C_d = C_{\text{non-circ}} + C_{\text{circ}} = \frac{\pi c}{2U_\infty^2} \ddot{h} + \frac{2}{U_\infty^2 c}(\dot{\Gamma} d + \Gamma \dot{d}) \tag{15}$$

Equation 15 presents the low-order force solution with the contribution from virtual mass and circulatory force, where the circulatory force component is influenced by both the growth of the vortices and the relative motion between LEV and TEV.

2.4.2 Modified model for surging motion

One limitation of the reduced-order model (Eq. 15) is that it only considers the accelerating motion of a flat plate, assuming that the motion is only in one direction. In the case of the surging wing, accelerations and decelerations occur, with the wing moving both upwind and downwind. In particular, a vortex pair is generated downstream of the wing during the upwind motion, as for the flat plate. Instead, during the downwind motion, depending on the reduced frequency k, vortices can also be generated upwind of the wing, resulting in a situation where both upwind and downwind vortices are present. In this case, Eq. 15 cannot be applied anymore. Let us consider, for instance, the case when the wing is moving downstream in a surging case, as illustrated in Fig. 6. The downstream motion of the wing causes the formation of two upwind

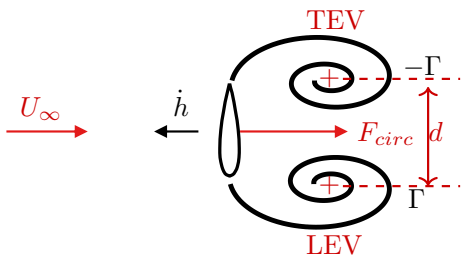

Fig. 5 Illustration of the airfoil's vorticity field and circulatory force moving in the upstream direction. Γ represents the absolute value of the circulation from LEV and TEV. "+" represent the vortex cores. F_{circ} represents the circulatory drag force

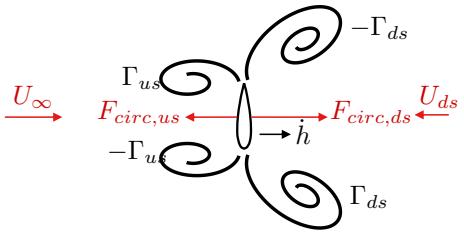

Fig. 6 Illustration of the airfoil's vorticity field and circulatory force moving in the downstream direction during a surging motion. The circulatory force and circulation are split into two groups. The ones with the underscore "us" represent the circulatory force and circulation generated by the wake velocity U_{ds} during the downwind motion of the wing. The ones with the underscore "ds" represent the circulatory force and circulation generated during the upwind motion of the wing

vortices of circulation (Γ_{us} and -Γ_{us}), whose contribution to the drag is $F_{circ,us}$. However, the wing is moving in a region of flow directed upstream at a velocity U_{ds}. In this flow region, two vortices are present, generated from the previous upwind motion of the wing, whose circulation is Γ_{ds} and -Γ_{ds}, which contribute to the drag force via $F_{circ,ds}$. Considering this situation in the flat plate model (Eq. 15), the circulatory force in the updated model is computed as the sum of the circulatory forces from each vortex pair. Thus, during the downstream motion in certain cases, the drag coefficient is calculated as:

$$C_d = (F_{\text{non-circ}} + F_{\text{circ,us}} - F_{\text{circ,ds}})/\left(\frac{1}{2}\rho U_\infty^2 c\right) \tag{16}$$

Using Eq. 10 to calculate $F_{\text{non-circ}}$ and Eq. 15 to calculate $F_{\text{circ,us}}$ and $F_{\text{circ,ds}}$, Eq. 16 becomes:

$$C_d = \frac{\pi c}{2U_\infty^2}\ddot{h} + \frac{2}{U_\infty^2 c}(\dot{\Gamma}_{\text{us}} d_{\text{us}} + \Gamma_{\text{us}} \dot{d}_{\text{us}} - \dot{\Gamma}_{\text{ds}} d_{\text{ds}} - \Gamma_{\text{ds}} \dot{d}_{\text{ds}}) \tag{17}$$

3 Results and discussion

3.1 Velocity and vortex dynamics

3.1.1 Static case

The static wing case is discussed first regarding velocity and vorticity fields. Figure 7 shows the time-averaged (from 200 samples) streamwise velocity $\bar{u}/U_\infty$ and vorticity $\bar{\omega}c/U_\infty$ field at $3c$ distance from the wing's tip, with the airfoil at AoA = 90°. The gray area in the plots represents the shadow region where the airfoil blocked the laser light from the bottom, as shown in Fig. 1; hence, no velocity measurement is possible in that region. At such large AoA, the airfoil generates a large wake, whose width scales with the airfoil's chord, where a significant flow reversal occurs (velocity up to about 0.3 of U_∞). Vortices are shed alternatively from the leading and trailing edges but are not visible in the mean flow field. Instead, high vorticity is present in the shear layers emanating from the leading and trailing edges.

Flow fields are captured $2.5c$ downstream of the wing to determine the vortex shedding frequency of the static wing. The distance is defined between the airfoil chord line to the left boundary of the FoV. Two instantaneous flow fields at t = 10.27s and = 15.65s are shown in Fig. 8a and b. In the figure, the vortex shedding from the leading edge and trailing edge is visible, resulting in a sinusoidal shape of the wake. Proper orthogonal decomposition (POD) analysis is performed on the flow fields to identify the most energetic modes associated with the wake dynamics (Smith et al. 2005). The first two modes feature a comparable energy content of 9.5% and 8.1% (as shown in Fig. 9) and are in quadrature of phase; the first two modes of the cross-flow velocity component v, shown in Fig. 8c and d, represent the convection of the streamwise vortices shed from the leading and trailing edges of the wing. The distance between the two neighboring peaks in the streamwise direction ($1.88c$) in Fig. 8c represents half of the wavelength of the vortex.

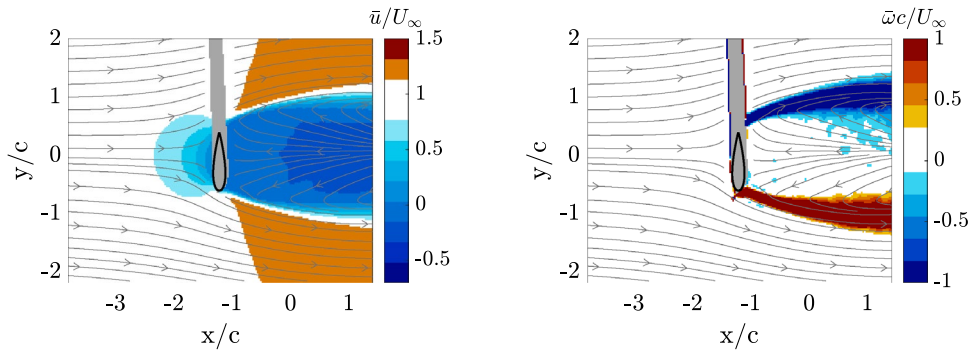

(a) $\bar{u}/U_\infty$ (b) $\bar{\omega}c/U_\infty$

Fig. 7 Streamwise velocity field $\bar{u}/U_\infty$ and vorticity field $\bar{\omega}c/U_\infty$ of the static wing at $3c$ location from the tip

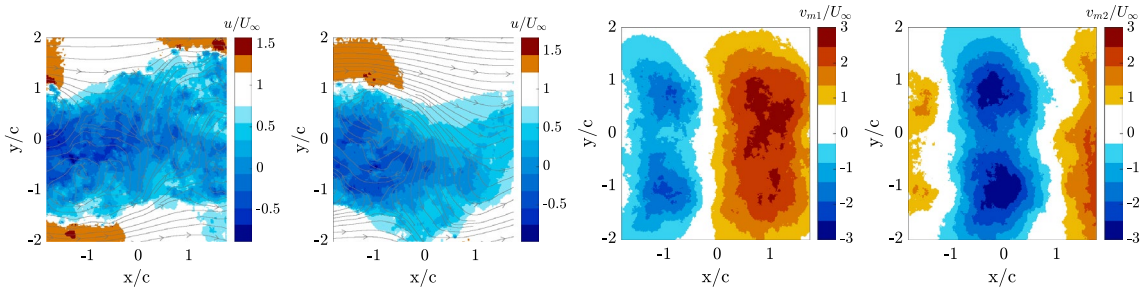

Fig. 8 Instantaneous streamwise velocity field u/U_∞ 2.5c downstream from the airfoil at **a** t= 10.27 s, (**b**) t= 15.65 s and the first two modes of the cross-flow velocity component v (**c**) and **d** from the POD analysis. Note that distance of the FoV with respect to the airfoil is defined as the distance between the airfoil chord line and the left boundary of the FoV

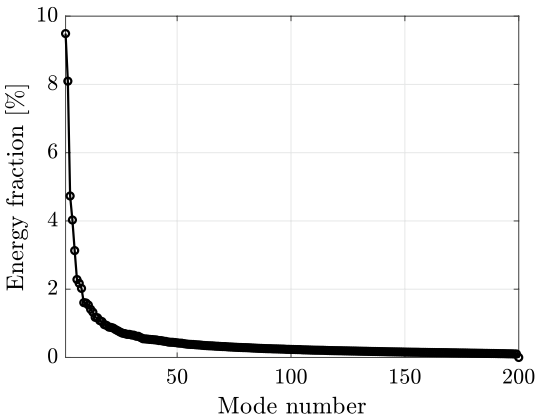

Fig. 9 Energy content at different mode number

Based on the convective velocity in the shear layer, which is estimated as 60% of the free stream, the vortex shedding frequency f_{st} for the static wing (defined as velocity divided by wavelength) is calculated as 6.4 Hz, resulting in a Strouhal number $St = f_{st}c/U_\infty = 0.159$.

3.1.2 Surging cases

The surging motion was conducted at 5 Hz and 2.5 Hz. Based on the f_{st} obtained from the static measurements, the corresponding frequency ratio of the motion frequency f with respect to f_{st} is 0.78 and 0.39. The phase-averaged streamwise velocity fields superimposed with streamlines are shown in Fig. 10 during a cycle of motion for the reduced frequency $k = 0.38$ (Animation provided in Online Resource 1). In total, 12 phases were captured, and the result is shown in a vortex formation order in the wake instead of the phase-increasing order. When the airfoil moves in the upstream direction (for instance, phases $\phi = 0°$ and 45°), the flow shares similarity with that of the static wing, even though with a stronger velocity deficit inside the wake and a larger flow acceleration outside of the wake. When the airfoil moves in the downstream direction, instead, a region of velocity higher than U_∞ is formed upwind of the wing, whereas the wake downwind of the wing elongates on the top and bottom of the wing in the upwind direction (see for instance phases $\phi = 180°$ and 225°). The phase-averaged vorticity fields superimposed with streamlines for the same k are shown in Fig. 11 (Animation provided in Online Resource 2). The green crosses in Fig. 11 represent the vortex cores identified using the $\Gamma 1$ method explained in the methodology section. For the $k = 0.38$ surging case, the vortex formation in the wake starts from $\phi = 270°$, where the airfoil is at the most downstream position. At this phase, the wing starts moving upwind from zero velocity; thus, a vortex pair starts to form at the leading and trailing edges. As the wing moves upwind, the vortices grow in size and strength, fed by the vorticity of the shear layers. The end of the vortex formation period can be determined through the circulation of each phase, which for the leading edge vortices is shown in Fig. 12. The circulation is calculated using Eq. 4, excluding the points where the vorticity has the opposite sign with respect to that of the vortex. For the $k = 0.38$ case, Γ reaches the maximum at $\phi = 80°$ (close to the most upwind location) and remains approximately constant afterward. From $\phi = 80°$(Fig.11g) to $\phi = 100°$ (Fig. 11i), the wake vortices increase their distance in the cross-flow direction, while shrinking their size in the streamwise direction. Before $\phi = 80°$, the vortex pair builds up and the vortex formation length (the distance between the airfoil and the vortex core) elongates. When the airfoil decelerates toward $\phi = 90°$, the trailing vortices decelerate, because their motion is obstructed by the airfoil itself. When the airfoil starts to move in the downwind direction ($\phi > 90°$), it induces an increase of pressure between the vortices: as a consequence, the vortices detach and move apart in the cross-flow direction. From $\phi = 90°$ (the most upstream position) onwards, as the airfoil moves downwind, the vortices

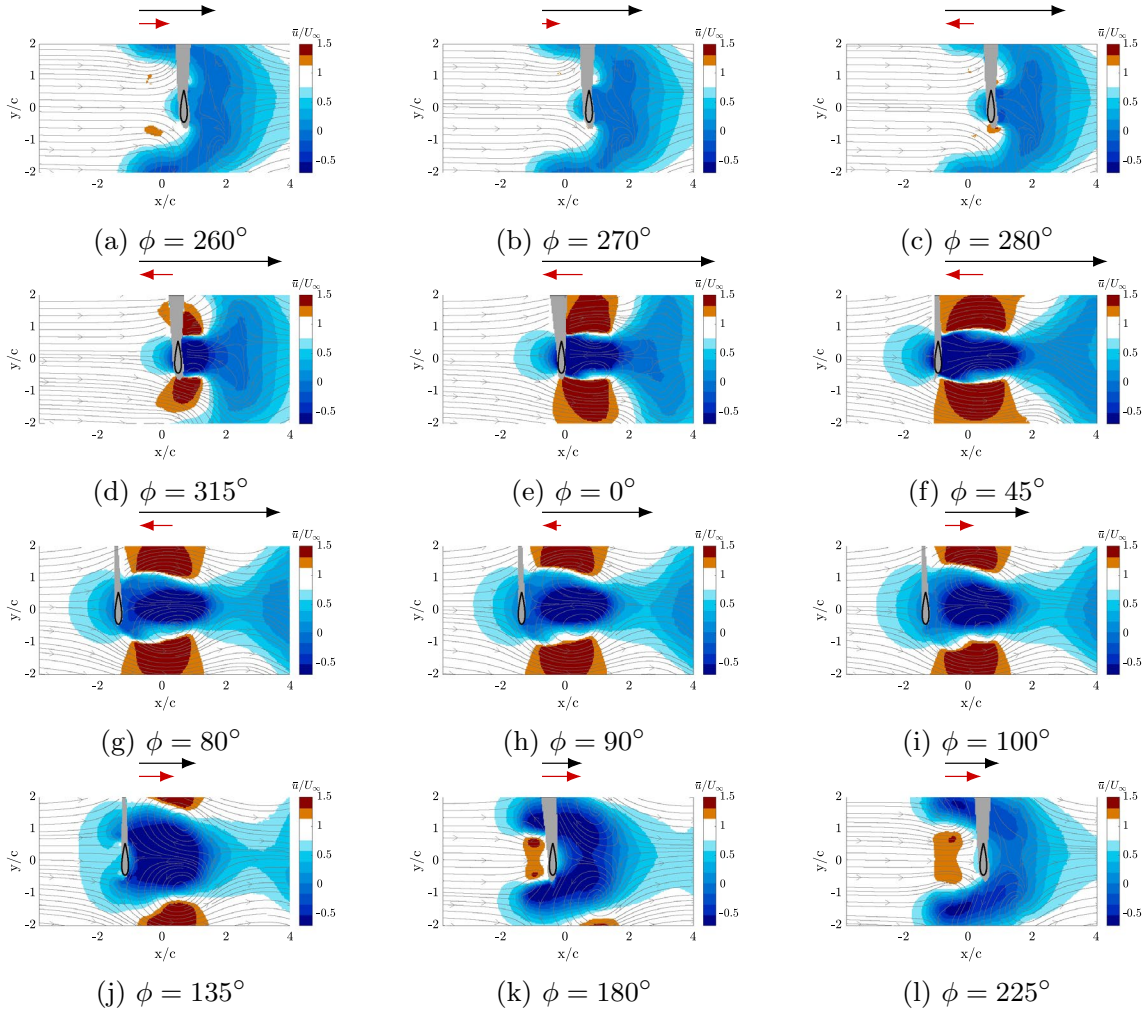

Fig. 10 Streamwise velocity field $\bar{u}/U_\infty$ for $k = 0.38$ surging case for all the measured phases. Instead of showing the increasing phase order, the same order as Fig. 11 is shown here. The black arrow represents the scaled relative velocity U_{rel} and the red arrow represents the scaled motion velocity $\dot{h}$. (Animation provided in Online Resource 1)

are pushed away from the airfoil, causing the vortex pair to detach from the airfoil's leading edge and trailing edge. This is identified by the fact that at 135°(Fig. 10j), the two vortices are cut off from the supply of fluid circulation from the shear layer connected to the airfoil leading and trailing edges.

Starting from $\phi = 135°$, another pair of starting vortices, in the upwind direction, starts generating and growing until $\phi = 225°$. At $\phi = 180°$, while the upwind vortices grow in size and strength, the downwind vortices gradually move away in the cross-flow direction from the wing. Similar to the downwind vortices, from $\phi = 225°$ the upwind vortices start to separate from the wing due to the deceleration of the latter. At $\phi = 280°$, they move away from the wing at a comparable speed as the downwind vortices. As the airfoil moves downstream, it moves within its own wake, characterized by low streamwise velocity generated during its upwind motion. With the relatively low incoming velocity and the relatively high wing motion velocity, the vortices shed upwind remain roughly at the same streamwise location during the donwnwind motion of the wing. It is noticed that one pair of downwind vortices (generated during the upwind motion) and one pair of upwind vortices (generated during the downwind motion) are shed simultaneously during one cycle of motion. Hence, it is concluded that, for the current case (frequency ratio $f/f_{\text{st}} = 0.78$), lock-in occurs between the vortex shedding and wing's motion.

Figure 13 displays the superimposed streamlines with streamwise velocity fields for all the measured phases for the $k = 0.19$ case (Animation provided in Online Resource 3). Compared with the $k = 0.38$ case, the wing's velocity is lower, meaning that the perceived wind of the airfoil is closer to the free-stream velocity; as a consequence, the resulting flow fields exhibit higher similarity to that of the static wing case shown in Fig. 7a. In particular, during the

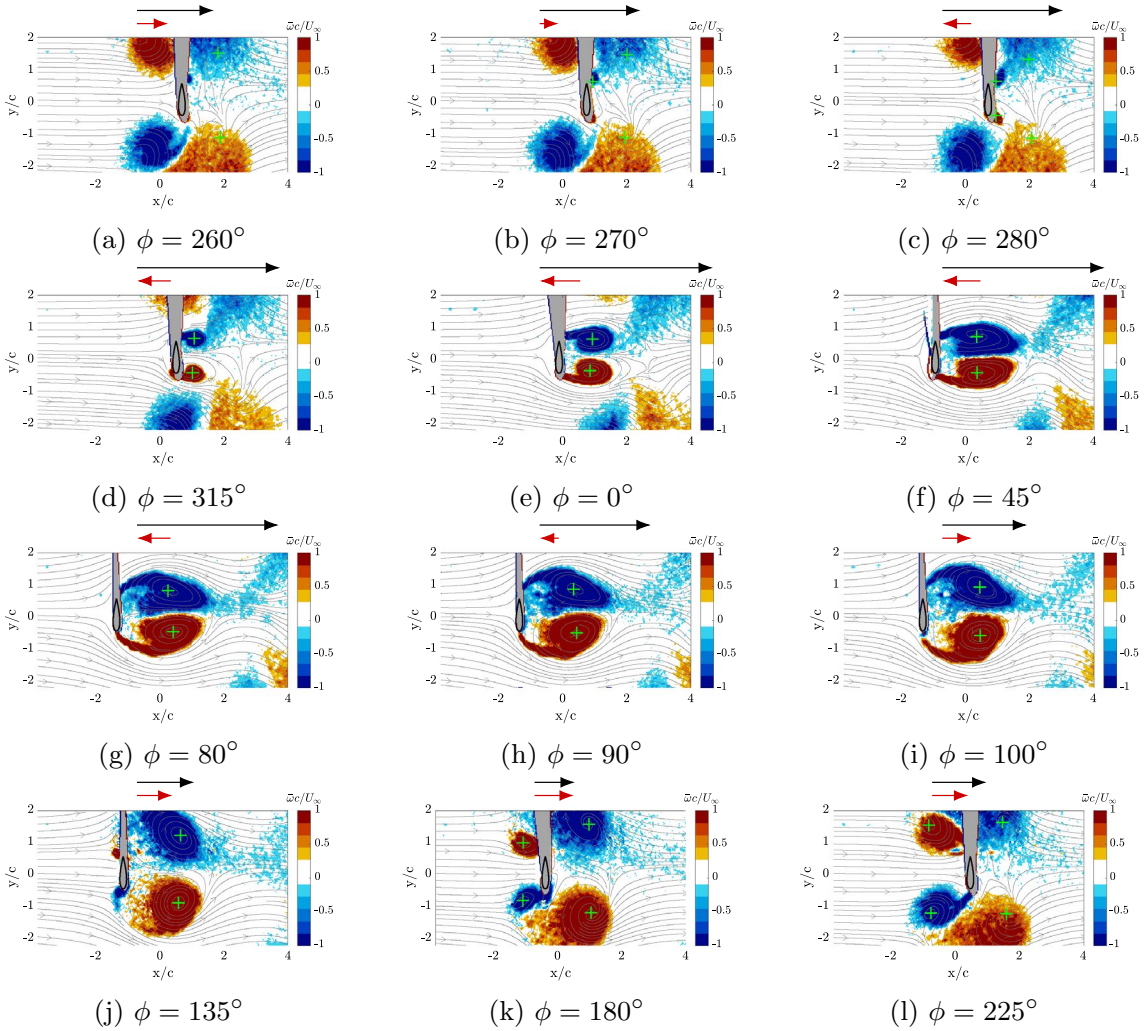

Fig. 11 Contours of the phase-averaged spanwise vorticity component superimposed with streamlines. Vortex identified using Γ_1 method for $k = 0.38$ surging case. The vortex center is marked as crosses in green. The black arrow represents the scaled relative velocity U_{rel} and the red arrow represents the scaled motion velocity $\dot{h}$. (Animation provided in Online Resource 2)

downwind motion of the wing (phases between $\phi = 90°$ and $\phi = 270°$), the wing's velocity is not high enough to move the downwind vortices laterally. Furthermore, the flow stagnation always occurs on the upwind side of the wing, whereas the wake is always on the downwind side. From the vorticity fields, illustrated in Fig. 14 (Animation provided in Online Resource 4), two main observations can be made: (i) contrary to the $k = 0.38$ case, vortices are shed only on the downwind side of the wing and not on the upwind side: this result is because the wing motion velocity is low compared with the free-stream velocity, hence no starting vortex is formed when the wing moves downwind; (ii) Although different from the $k = 0.38$ case where two pairs of vortices (one pair upwind and one pair downwind) shed, at $k = 0.19$, during one period of motion, only one pair of counter-rotating vortices is shed, which indicates a different form of lock-in between the wing motion and the vortex shedding. The first observation implies that the motion kinematics of the wing dominates the upwind vortex shedding, thus highlighting the importance of motion-reduced frequency on the flow dynamics. From the measured data, the start of the vortex generation is at $\phi = 225°$, where a pair of small vortex blobs starts to form downstream of the airfoil. From Fig. 12, it is noticed that, for the $k = 0.19$ case, Γ increases until $\phi = 90°$ and decreases afterward. At $\phi = 135°$, it is observed that the vorticity exhibits a "noisy" pattern between $x/c = 1$ and 2. Although this is ascribed to the limited ensemble size (it is reminded that the phase-average flow fields were obtained from 200 instantaneous fields), it indicates that the wake vortices are not stable and dissipate to the surrounding flow. At $\phi = 180°$, the vorticity is spread in a larger area, and only the leading edge vortex core can be found in the measurement domain. Compared with $k = 0.38$ case, when the wing is moving upwind, the wake generated in the $k = 0.19$

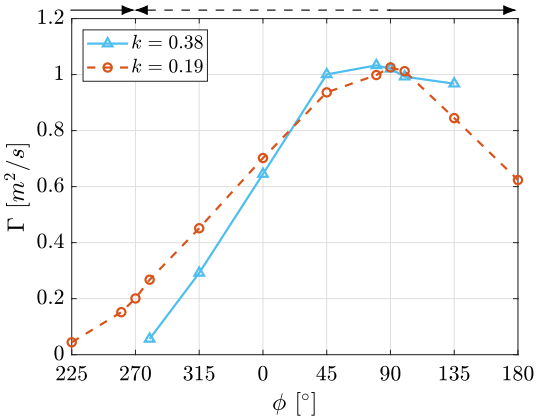

Fig. 12 Circulation Γ of the wake vortex in the downstream side from the leading edge at different phases in a cycle. The solid horizontal arrow pointing right on top of the plot represents the downstream motion, and the dashed arrow pointing left represents the upstream motion of the airfoil

case is downwind of the wing, similarly to the $k = 0.38$ case. However, in the latter case, a higher reverse velocity is encountered. In this condition, when the airfoil moves back in the downwind motion, the energy that the wing feeds into the flow combines with the energy of the wake flow: because of the lower wing velocity in the $k = 0.19$ case, the wake remains downwind of the wing, contrary to the $k = 0.38$ case, where the wake elongates to the sides and upwind of the wing. It is noticed that, in the $k = 0.19$ case, the vorticity field is significantly different from that of the $k = 0.38$ case, indicating that k influences the vortex dynamics to a large extent. On the other hand, the second observation (namely the fact that only one pair of counter-rotating vortices is shed during one motion cycle under this frequency, which is different from the $k = 0.38$ case where two pairs of vortices are generated and shed simultaneously during one cycle, only one pair of counter-rotating vortices is shed) indicates that even though the two motion cases have different vortex dynamics, they all eventually feature the lock-in effect. While the lock-in from the high reduced frequency is expected due to f/f_{st} close to unity, the lock-in in the low reduced frequency case is ascribed to the large motion amplitude. The simulation results from Choi et al. (2015) of an oscillating airfoil indicate that lock-in occurs for small motion amplitudes for f/f_{st} closes to unity. In contrast, for large motion amplitudes, it can also occur for sub-harmonics, e.g., $f/f_{st} = 0.5$. In the present test case, for the low reduced frequency ($k = 0.19$) case, the frequency ratio is $f/f_{st} = 0.39$, which, given the motion amplitude of $1.1c$ yields a lock-in between frequency of motion and vortex shedding.

Figure 15 presents the trajectory of the downwind leading edge vortex along a cycle. The vortex core is identified using the Γ_1 method explained in the previous section. Starting from the beginning of the vortex formation ($\phi = 280°$ for $k = 0.19$ case and $\phi = 260°$ for $k = 0.38$ case) to $\phi = 45°$, the motion in the streamwise direction follows the sinusoidal shape. For both the reduced frequencies, up to $\phi = 315°$, the vortex moves slightly downstream because of the free-stream velocity in the downwind directions; for successive phases up to $\phi = 45°$, the vortex moves upstream instead, subject to the flow velocity induced by the upwind motion of the wing. Clearly, such displacement is significantly larger for the $k = 0.38$ case due to the higher speed of the wing. From $\phi = 45°$, the vortex moves downstream because of the decreasing wing velocity (up to $\phi = 90°$) and its successive motion in the downwind direction (from $\phi = 90°$ onward). When looking at the transverse displacement of the vortex (along the y direction, illustrated in Fig. 15b), it can be seen that, for the lower reduced frequency $k = 0.19$, the vortex gradually moves away from the airfoil starting from phase $\phi = 315°$. Instead, at the higher reduced frequency $k = 0.38$, the vortex transverse position remains approximately constant up to $\phi = 45°$; afterward, the vortex quickly moves away from the wing due to the high wing velocity that has the effect of displacing the vortex in the vertical direction.

3.2 Load estimation

3.2.1 Static case

The load estimation method based on Eq. 5 to Eq. 6 is applied to the static wing first; in this case, because the wing is static and the time-average flow field is considered, the time derivative term in Eq. 6 is null. The pressure field is shown in Fig. 16a. The pressure field is non-dimensionalized as $C_P = (P - P_\infty)/(1/2\rho U_\infty^2)$, where P is the static pressure in the flow field and P_∞ is the free-stream pressure. The shadow region at the top of the airfoil, present in the velocity fields, was interpolated to allow for the pressure calculation using the Poisson equation. It is important to note that, although the shaded area is present, it primarily remains outside the wake region. For the sake of computation of the aerodynamic loads via Eq. 6, linear interpolation of the velocity at the boundaries at the shaded region is performed. Because in the shaded region, the flow is mainly a potential flow, and because the aerodynamic loads are evaluated from the line integral along the control boundaries, the uncertainty associated with this interpolation is deemed negligible. Upwind of the wing, the flow field clearly follows potential flow theory: As the wind approaches the airfoil, the speed decreases and the pressure increases, based on Bernoulli's principle. Instead, downstream of the airfoil, a wake is present, where C_P is lower than 0 due to the presence of wake vortices and reverse flow. The corresponding force contributions from mean convection (MC), pressure

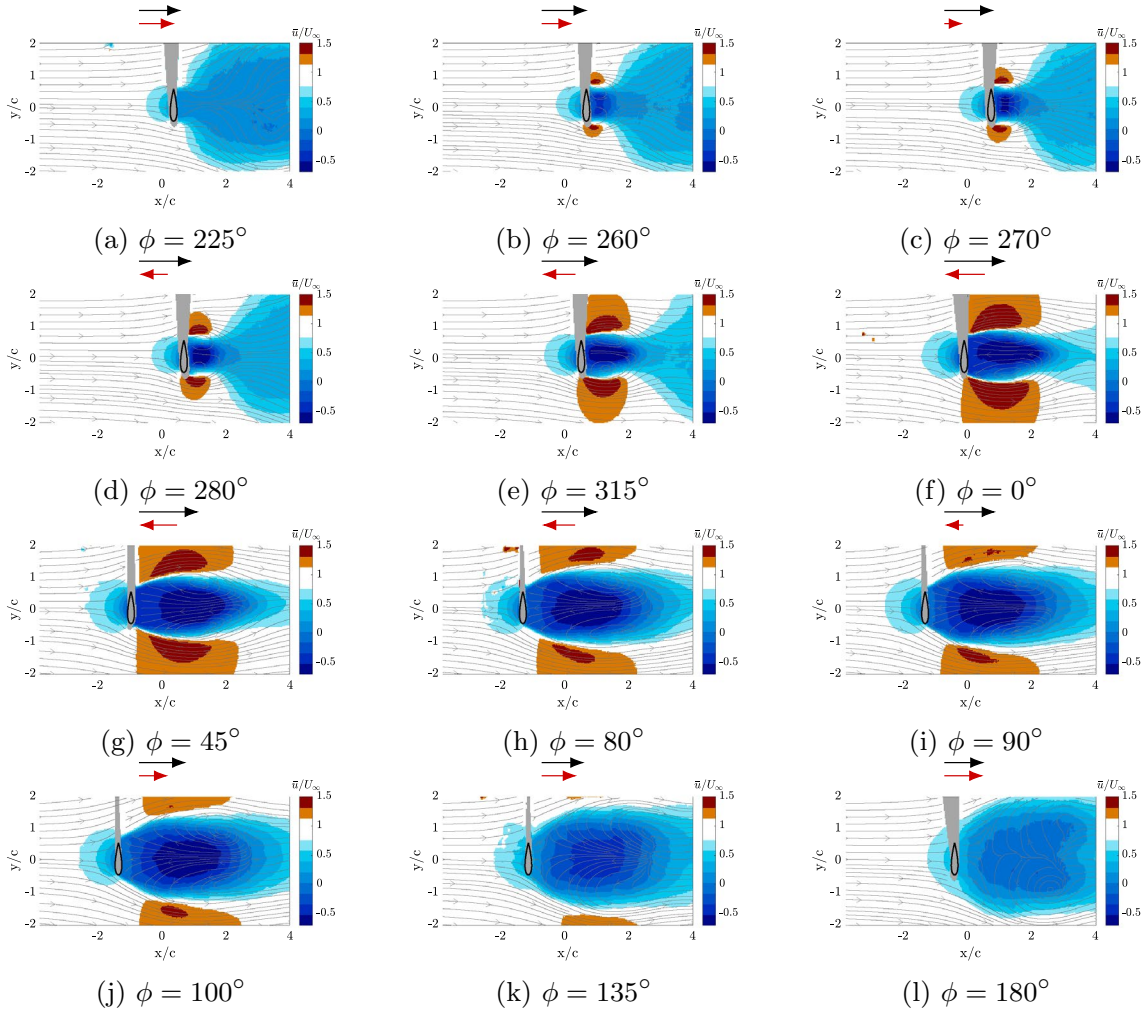

Fig. 13 Streamwise velocity field $\bar{u}/U_\infty$ for $k = 0.19$ surging case for all the measured phases. Instead of showing the increasing phase order, the same order as Fig. 14 is shown here.The black arrow represents the scaled relative velocity U_{rel} and the red arrow represents the scaled motion velocity $\dot{h}$. (Animation provided in Online Resource 3)

(press) and turbulence momentum transfer (TMT) are shown in Fig. 16b. Note that the positive or negative sign in front of each term in Eq. 6 is included in the force component. The mean viscous stress term is not included in the bar plot because it is several orders of magnitude lower than the others. Also, for the static case, the body force term is zero. For the calculation of the force contributions via Eq. 6, a control contour around the airfoil shall be defined. The control contour surrounding the airfoil, shown in Fig. 16a, extends from 10 dx to 30 dx from the airfoil surface, where d$x = 0.027c$ represents the streamwise grid spacing. Error bars of forces determined using the different control contours are added to the bar plot of Fig. 16b, whose sizes represent the uncertainty at 95% confidence level. From the load result of 21 different control contours, the drag coefficient C_{d} is obtained with a mean value of 0.95 and a 95% confidence interval of 0.01. The pressure term provides the only positive contribution to the total force, while MC and TMT give a negative contribution, which is ascribed to the fact that all control contours are relatively close to the airfoil. As the airfoil stands as the bluff body in the flow at AoA 90°, the pressure force from the flow acts mainly horizontally, that is, normal to the chord line, thus giving rise to a relatively high-pressure drag. The contribution of MC to the control contour boundary is shown in Fig. 17. The control contour showcased has a fixed 20 dx distance from each boundary of the airfoil surface. The curve starts from the bottom-left of the control contour; The dashed lines represent the boundary of the turning point in the control contour. Note that for the rest of the discussion, the control contour follows the same as here. The figure shows that even though the front boundary has a positive contribution from MC due to the deceleration of flow in front of the airfoil, the top, bottom, and back boundaries provide a negative contribution due to

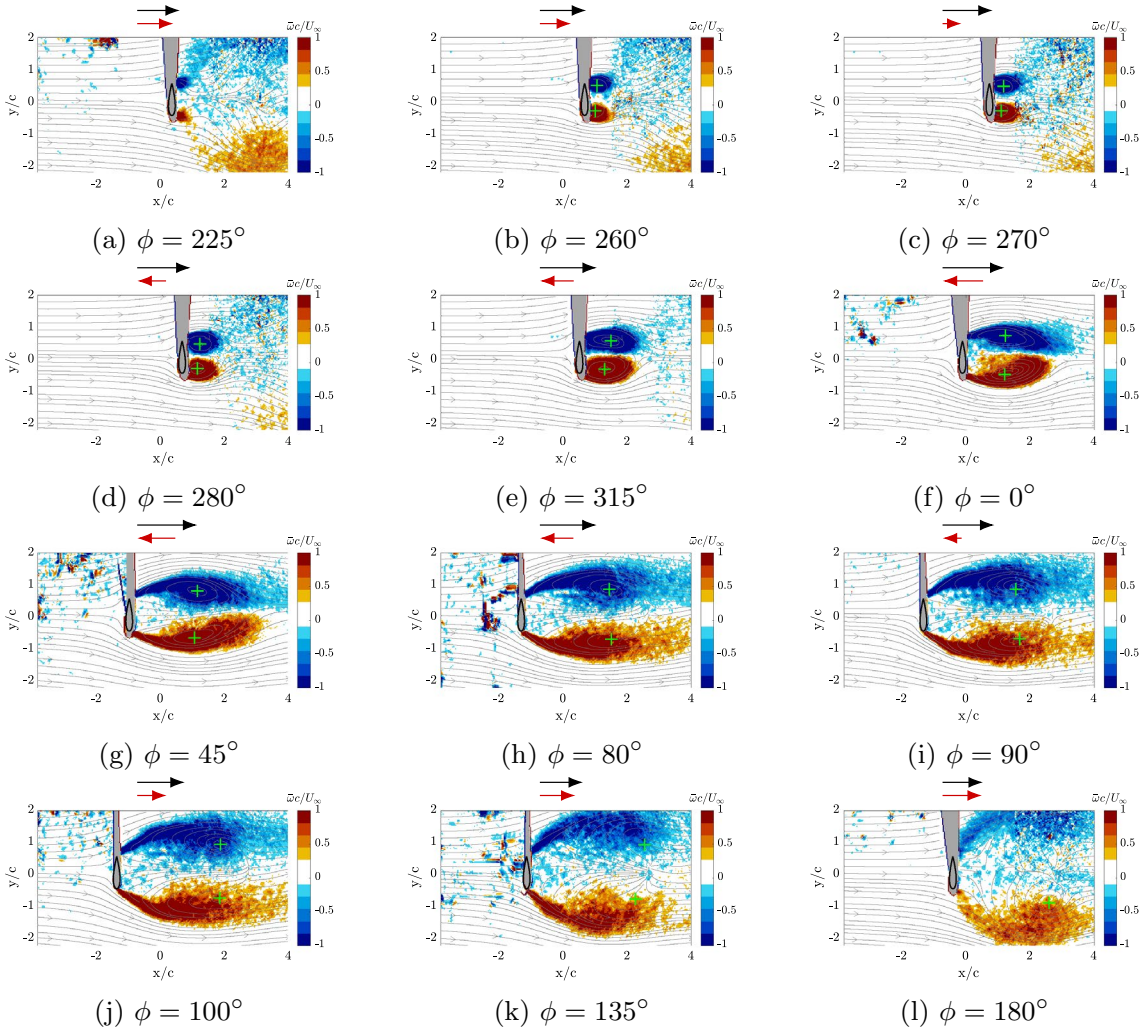

Fig. 14 Contours of the phase-averaged spanwise vorticity component superimposed with streamlines. Vortex identified using Γ_1 method for the $k = 0.19$ surging case. The vortex center is marked as crosses in green. The black arrow represents the scaled relative velocity U_{rel} and the red arrow represents the scaled motion velocity $\dot{h}$. Note that for $\phi = 225°$, this method cannot recognize the vortices near the leading edge and trailing edge of the airfoil as the small vortices are near the shadow region. (Animation provided in Online Resource 4)

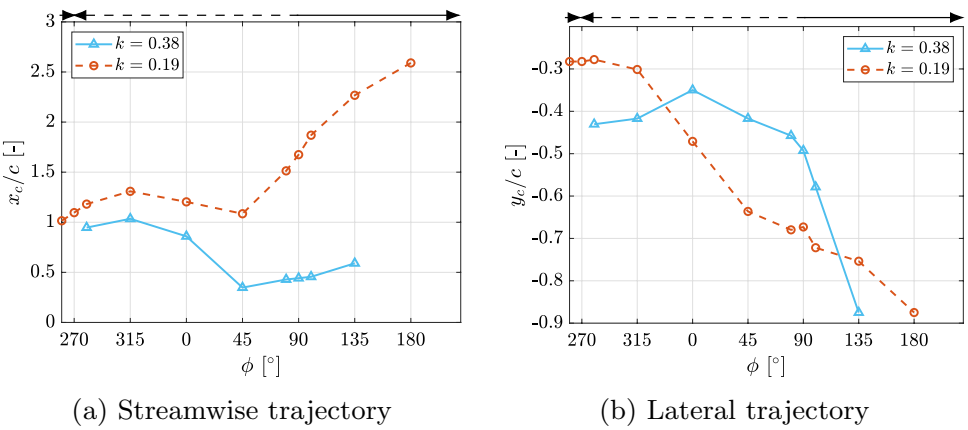

(a) Streamwise trajectory (b) Lateral trajectory

Fig. 15 Streamwise and lateral trajectory of the leading edge vortex core (in the order of vortex formation) for $k = 0.38$ and $k = 0.19$ surging motions. Only the core of the downwind vortex is considered. The solid horizontal arrow pointing right on top of the plot represents the downstream motion, and the dashed arrow pointing left represents the upstream motion of the airfoil

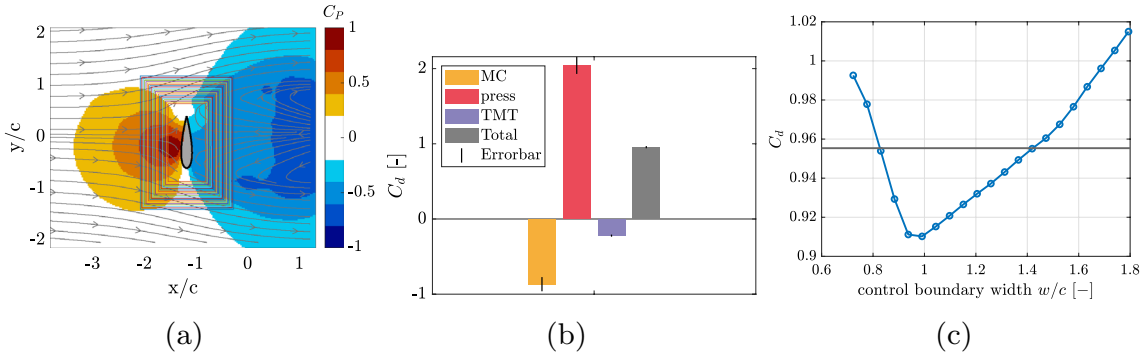

Fig. 16 **a** Pressure field of the static blade at 3c location from the tip. The control contour outside of the airfoil in Fig. 16a ranges from 10 dx to 30 dx from the airfoil surface, with dx = 0.027c. Re Force contribution from mean convection (MC), pressure (press) and turbulence momentum transfer (TMT) for the static case. The errorbar height represents the uncertainty at 95% confidence level. **c** C_d as a function of control boundary length, where the black horizontal line is the mean value

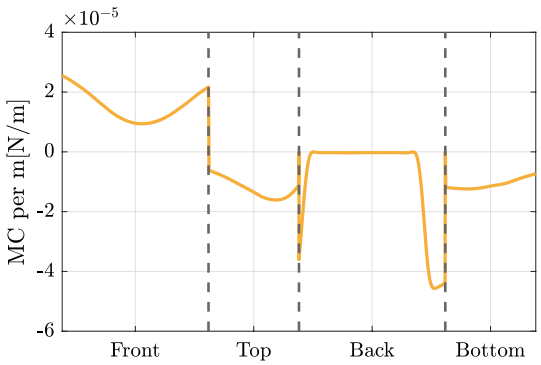

Fig. 17 Force component from mean convention (MC) on the control contour for the static measurement. The control contour presented here has a fixed 20 dx distance from each boundary of the airfoil surface. The curves start from the bottom-left of the control contour. The dashed lines represent the boundary of the turning point in the control contour

the accelerated flow at the top, bottom, and downwind of the airfoil outside the shear layer (Fig. 7a).

In order to examine the validity of the load estimation method, C_d obtained from each control boundary is plotted against the control boundary width w/c in Fig. 16c. The black horizontal line represents the mean value. It is shown that as w/c increases, C_d first decreases, reaching a local minimum and then increases again. Therefore, the result does not show a convergence related to the control boundary. Firstly, when the control boundary is too small, the relatively high velocity gradients near the airfoil cause larger uncertainty in the local pressure value and in turn in the estimated load. Secondly, as we neglect the spanwise flow in the load estimation method, the mass and momentum are not preserved in the two-dimensional control boundary. As a result, the larger the control volume, the less two-dimensional mass and momentum conservation are expected to hold. This poses a limitation to the method used here. However, it is further noted that the error for the total drag coefficient is smaller than the error from MC and pressure, indicating that the momentum and pressure terms are more influenced by the control volume boundary while the total drag coefficient is minimally affected due to the cumulative contribution of all forces. The variation of C_d in the range of considered contours is approximately 5% to 10%, which is much smaller than the variation of C_d at the different phases of the surging motion cases (discussed later). Thus, the average C_d is used to represent the mean value of the tests.

To validate the result, measurements reported in the literature have been reviewed. Even though this airfoil profile has been widely studied, the large angle of attack case is rarely considered. Experimental load measurements can be found in Holst et al. (2019). In their study, load measurements were conducted at AoA 90° and Re = 1.4×10^5, from which a drag coefficient of 0.87 was computed. However, the C_d obtained from this campaign is 0.95 for a lower Re of 1.5×10^4. In the wind tunnel measurement by Xu et al. (2024), a DU91 airfoil was tested with three different Re numbers. The results showed a slightly higher C_d at the lowest Re value of 2×10^5, compared to the other two values (Re = 5×10^5 and Re = 8×10^5) at AoA 90°. Thus, the effect of Re is one of the contributing factors to the difference in Cd compared with the result of Holst et al. (2019). Apart from this, both campaigns use an open jet, while two end plates were applied to the airfoil for the campaign by Holst et al. (2019), whereas only one end plate was applied for this campaign. This may induce some three-dimensional effects in our campaign, where the spanwise velocity is not zero. Regarding uncertainty, the difference between the experimental measurements by Holst et al. (2019) and the integration method presented here mainly stems from (1) the uncertainty of the PIV measurements compared to the pressure measurements and (2) the uncertainty in the interpolated

shadow region in the PIV data. Since uncertainties and three-dimensional effects are inevitable in this campaign, the results from the integration method are considered valid for the dynamic case measurements.

3.2.2 Surging cases

The load estimation method was then applied to the surging motion case. Figure 18a presents the C_d as a function of the motion phase, whereas Fig. 18b presents the C_d as a function of the wing's position. For both plots, the shaded area represents the 95% confidence interval based on all the control contours tested. The solid lines in Fig. 18b represent the airfoil moving in the upwind direction, while the dashed curves represent the airfoil moving in the downwind direction. The gray line in both plots represents the static C_d value. As the 95% confidence interval is rather small for the static case, it cannot be seen in the plot.

Figure 18a shows that the highest C_d occurs at $\phi = 0°$ for both reduced frequencies. At this phase, the airfoil is at the center of the travel and is moving upstream, bringing high momentum in the direction opposite to the free stream, thus resulting in the highest relative velocity perceived by the airfoil. In this case, the surging motion at $k = 0.38$ has 3 times the C_d compared with the static case, whereas for the $k = 0.19$ motion, the C_d is 2.4. This result emphasizes the importance of studying the wing dynamics because the wing's motion can yield force coefficients that are several times larger than the corresponding static ones.

For most of the tested phases, the drag force is positive, meaning that it is directed downstream (same direction as the free-stream velocity). However, around $\phi = 135°$, C_d has a negative value, which means that the drag force is directed upwind. The force contribution in the streamwise direction from MC, press, TMT, and TD on the control contour is shown in Fig. 19. Note that the viscous force and the body force term are not included and will not be included in the discussion as they are relatively small compared to the rest of the force terms. At this phase, the flow field (Fig. 10j) shows that, as the airfoil moves downwind, the downwind side still preserves the reversed flow from the previous upstream motion. As a result, the flow at the back of the airfoil potentially pushes the airfoil in the upwind direction, thus creating a considerable force toward the upwind. This leads to the substantial negative contribution from MC at the back boundary. Conversely, Fig. 19 shows that the pressure term has a positive contribution to the total C_d. In addition, the TD term has a negative contribution to the total C_d; in fact, it can be seen from the figure that the major part of the

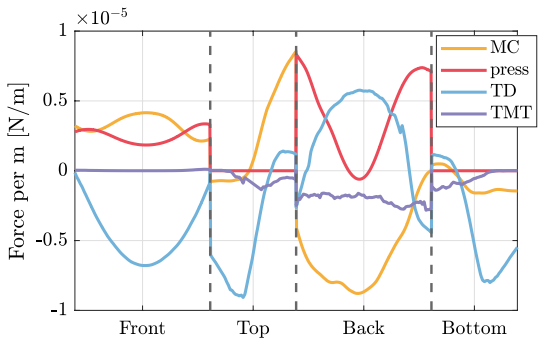

Fig. 19 Force component from mean convention (MC), time derivative (TD) and turbulence momentum transfer (TMT) on the control contour for $\phi = 135°$, $k = 0.38$ case. The control contour presented here has a fixed 20 dx distance from each boundary of the airfoil surface. The curves start from the bottom-left of the control contour. The dashed lines represent the boundary of the turning point in the control contour

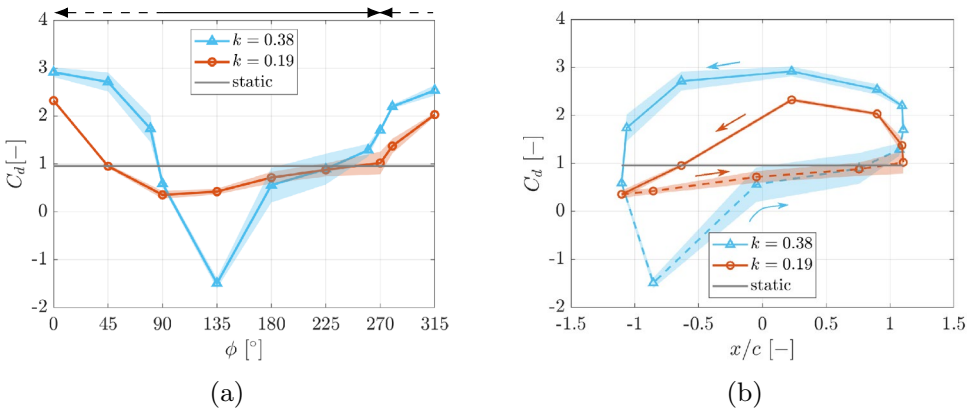

Fig. 18 Drag coefficient C_d **a** at each phase and **b** at each location. The shaded area represents 95% confident intervals of the mean value. The horizontal line in the plot represents the static C_d. The solid horizontal arrow pointing right on top of the plot represents the downstream motion, and the dashed arrow pointing left represents the upstream motion of the airfoil. Note that the shaded area for the static case is barely visible as the value is small. Solid lines in **b** represent the airfoil moving in the upstream direction and the dashed lines in **b** represent the airfoil moving in the downstream direction. The arrows represents the direction of the motion

TD curve is below zero, including the front boundary, and the parts of the top and bottom boundary which are in the upwind of the airfoil. This is because at this phase, when the airfoil is moving downstream, the flow in the upwind part of the airfoil is accelerated, as can be seen from Fig. 10i –k. At the back of the airfoil, due to the vortex shedding process (see Fig. 11i– k), the vortices are moving away from the airfoil in the cross-flow direction, creating a larger area of deep reverse flow. This leads to the positive TD term at the back part of the boundary. The TMT term is almost zero in the upwind direction of the airfoil, due to the almost parallel incoming wind. It has a negative value at the top, bottom, and especially back due to the airfoil encountering reverse flow, which increases the Reynolds stresses. Therefore, by adding up all the contributions from the force, the total drag coefficient is negative despite the positive contribution from the pressure.

In a different perspective, Fig. 18b shows the C_d hysteresis in the wing's motion loop. The kinematics highly influences the variation of C_d in a loop. The hysteresis loop has a larger amplitude difference for $k = 0.38$ compared to $k = 0.19$. This result also follows the trend from the result of Choi et al. (2015), where the slender loop represents the sub-harmonic lock-in and the more round loop represents the lock-in when f/f_{st} gets close to unity. During one motion cycle, the sub-harmonic lock-in presents a flow field closer to the steady case than the higher k case. The wake vortices grow only at the downwind side of the airfoil. In contrast, for the higher frequency case ($k = 0.38$), wake vortices form on both sides of the airfoil, resulting in greater flow variability. This increased variation amplifies the hysteresis loop compared to the lower frequency case ($k = 0.19$). Specifically, when the airfoil moves in the downstream direction, it moves into its own wake. Thus, the relative wind speed is much lower than the free-stream velocity. As a result, the vortices are shed toward the upstream direction for phases from $\phi = 135°$ to $\phi = 280°$, leading to a high difference with the upstream motion case.

The results of the force components from time derivative (TD), mean convection (MC), turbulence momentum transfer (TMT), and pressure (press) are shown in Fig. 20 for the two reduced frequencies. The mean viscous stress term and the body force term are not included in the bar plot as they have relatively small contributions. The error bar height represents the 95% confidence intervals from all the control contours tested. Comparing the two frequencies, the case with $k = 0.38$ exhibits a significantly higher C_d for each force component. For instance, at $\phi = 0°$, both the MC and pressure terms are approximately twice as large for $k = 0.38$ compared to the $k = 0.19$ case, further confirming that the flow dynamics greatly affect the aerodynamic loads. Despite this, the periodic motion causes the force contributions to

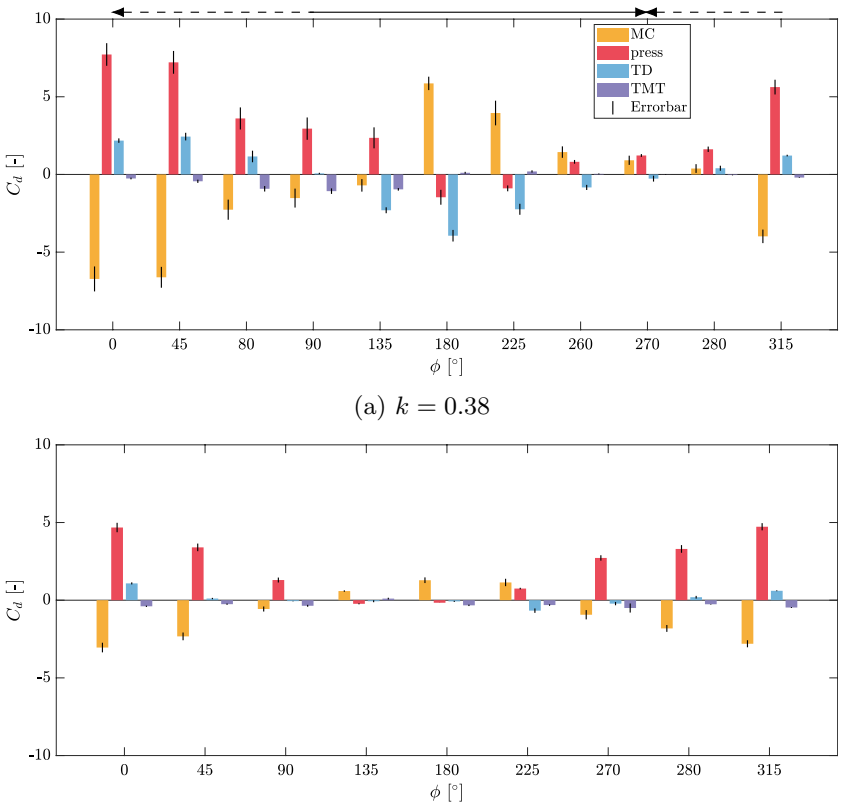

(a) $k = 0.38$

(b) $k = 0.19$

Fig. 20 Aerodynamic force contribution at $k = 0.19$ and $k = 0.38$ from mean convection (MC), pressure (press), turbulent momentum transfer (TMT), and time derivative (TD). The errorbar height represents the 95% confidence intervals. The solid horizontal arrow pointing right on top of the plot represents the downstream motion, and the dashed arrow pointing left represents the upstream motion of the airfoil

follow a distinct trend over each cycle for both motion frequencies, particularly for the MC and pressure terms. The MC term increases from $\phi = 0°$ to $\phi = 180°$, then decreases until the cycle's end (see Fig. 20). In contrast, the pressure term peaks at $\phi = 0°$, decreases to $\phi = 180°$, and then rises again by the cycle's completion. Since both frequencies exhibit the same trend for the main force component, the force components at $\phi = 0°$ and $\phi = 180°$ are compared as representative cases for $k = 0.38$ only.

The MC term, pressure term, and TD term are shown in Fig. 21. The MC term on the boundary (Fig. 21a) reveals that at $\phi = 0°$, when the airfoil is moving against the wind, a velocity deficit forms at the rear of the airfoil. In contrast, at $\phi = 180°$, when the airfoil moves downwind, the accelerated velocity at the front of the airfoil (as shown in Fig. 10k) leads to an MC deficit along the front boundary, albeit with smaller amplitude. Additionally, as the flow accelerates at $\phi = 0°$ and decelerates at $\phi = 180°$ along the top and bottom boundaries (see Fig. 10e and k), the MC force contributes negatively at these boundaries for $\phi = 0°$ and positively for $\phi = 180°$.

The pressure term in the streamwise direction (Fig. 21b) is derived from the pressure field of the two cases shown in Fig. 22. At the front of the airfoil, $\phi = 0°$ exhibits high positive pressure on the pressure side, while at $\phi = 180°$, the front serves as the suction side, resulting in negative pressure contribution. Conversely, at the back of the airfoil, $\phi = 0°$ has a reverse flow region that induces negative pressure. However, this negative pressure adds to the positive pressure term due to its sign in Eq. 6, as illustrated in Fig. 21b. For $\phi = 180°$, positive pressure is present on the airfoil surface, leading to a negative contribution in the central part of the back boundary. Although shed vortices create negative pressure, resulting in a positive contribution at the sides of the back, the overall pressure force term remains negative.

The TD term on the boundary, shown in Fig. 21c, is calculated using the first term in Eq. 6 and is obtained from its two adjacent phases. Due to the negative sign in the front, the decelerating flow from $\phi = 315°$ (Fig. 10k) to $\phi = 45°$ (Fig. 10f) in the front and wake region of the airfoil results in a positive contribution to the TD at $\phi = 0°$. In contrast, the accelerating flow from $\phi = 135°$ (Fig. 10j) to $\phi = 225°$ (Fig. 10l) in the same region leads to a negative contribution to the TD at $\phi = 180°$. By analyzing the three most dominant force components – MC, pressure, and TD– from the two extreme motion phases, it emerges that due to the difference in the flow dynamics, the force components take opposite effects on these two phases, which results in different total C_d as shown in Fig. 18b.

The non-dimensionalized aerodynamic power P* is shown in Fig. 23. It is calculated as $P* = C_d\dot{h}/(h_{max}f)$, where C_d is the drag coefficient, h_{max} is the motion amplitude, and f is the motion frequency. If P* is positive, it means the force is in the same direction as the motion, indicating

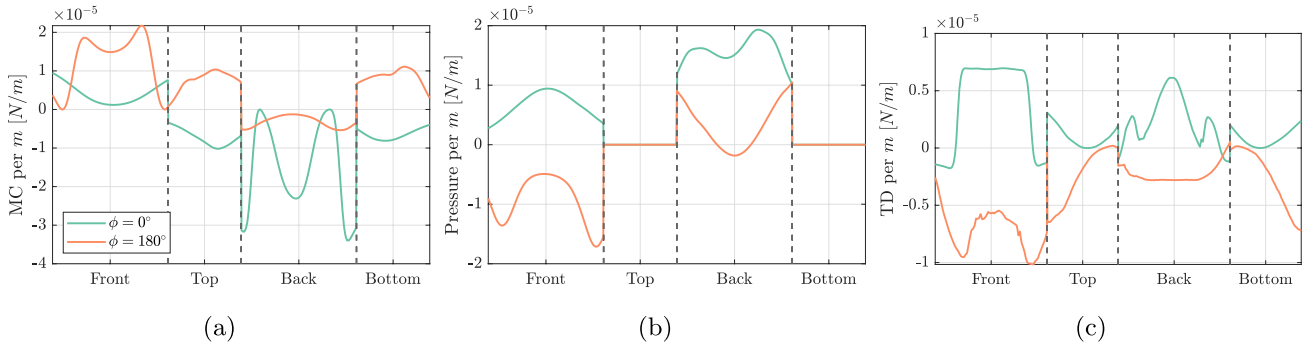

Fig. 21 MC **a**, pressure term **b**, and TD term **c** in the streamwise direction in Eq. 6 for $\phi = 0°$ and $\phi = 180°$ at $k = 0.38$

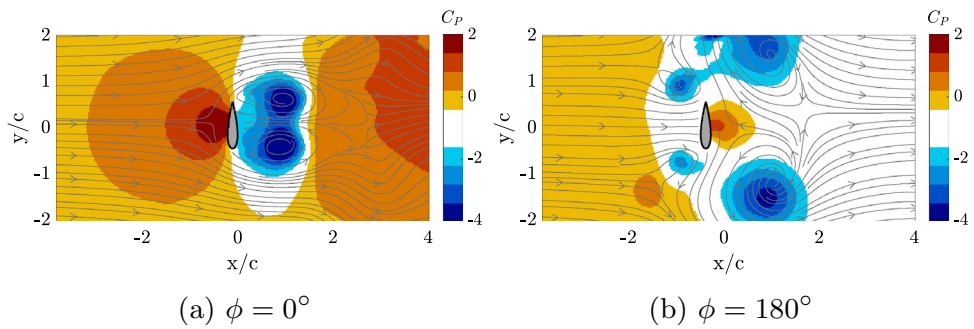

Fig. 22 Pressure field for **a** $\phi = 0°$ and **b** $\phi = 180°$ at $k = 0.38$

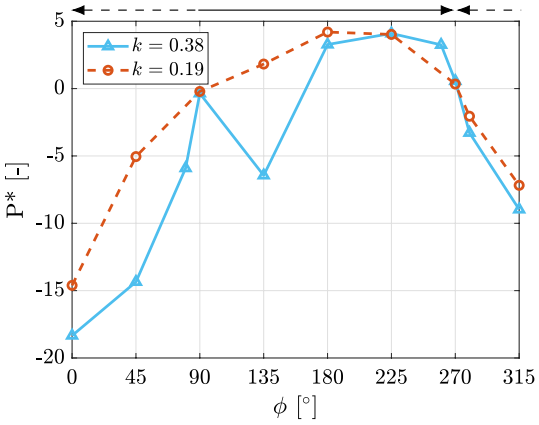

Fig. 23 Non-dimensional aerodynamic power P* in a cycle. P* is calculated as: $P^* = C_d\dot{h}/(h_{max}f)$, where C_d is the drag coefficient, h_{max} is the motion amplitude and f is the motion frequency. The solid horizontal arrow pointing right on top of the plot represents the downstream motion, and the dashed arrow pointing left represents the upstream motion of the airfoil

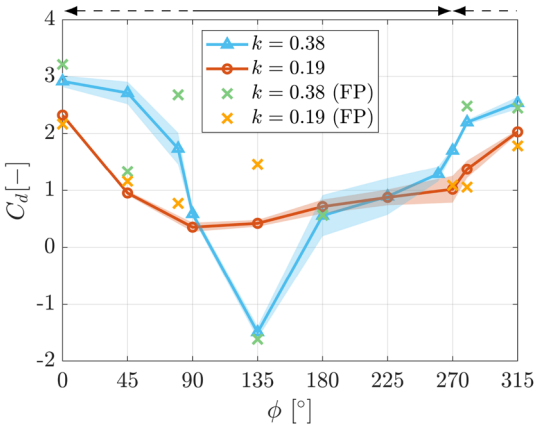

Fig. 24 Drag coefficient from control contour approach(Eq. 6) and from the modified flat plate (FP) model (Eq. 17). The solid horizontal arrow pointing right on top of the plot represents the downstream motion, and the dashed arrow pointing left represents the upstream motion of the airfoil

that the flow does positive work on the airfoil. Conversely, if P* is negative, the aerodynamic force is acting in the opposite direction of the motion. In this case, the airfoil does positive work on the flow. This means that the flow does negative work on the airfoil in this period instead. This definition of dimensionless power is the same as that introduced in Skrzypiński et al. (2013). Before $\phi = 90°$ and after $\phi = 280°$, P* is below zero for both the motion cases, meaning the airfoil does work on the flow. As a consequence, this phase range is characterized by the vortex growing period where continuous energy is fed to the vortices, which increases their strength. Between $\phi = 90°$ and $\phi = 180°$, instead, P* has positive values for the $k = 0.19$ motion cases, which means the airfoil extracts energy from the wind. As a result, this phase range is characterized by vortex shedding, where the flow loses energy to sustain the vortices. From $\phi = 180°$ to $\phi = 270°$, P* still remains positive for $k = 0.19$ motion case. In this phase range, the vortex motion is the combination of vortex shedding in a larger area in the downwind side and vortex growing in a smaller area in the closer downwind side. This means that the energy the airfoil extracts from the flow (that causes vortex shedding) is higher than the work the airfoil does on the flow (that causes vortex growing). For the $k = 0.38$ case, $\phi = 135°$ has negative P*. The flow at this phase is composed of vortex shedding in the downwind side and vortex growing in the upwind side. On the energy level, it means that the airfoil feeds more energy to the wind for the vortex growing than extracting the energy from the wind for the vortex shedding. Afterward, at $\phi = 180°$, P* returns to positive values again. Although the basic flow features are similar to those at $\phi = 135°$, the key difference is that the upwind vortices at $\phi = 135°$ are part of the start-up period. This suggests that, while the generated upwind vortices continue to grow during this phase (extracting energy from the airfoil and causing P* to decrease), the positive P* at $\phi = 180°$ indicates that less energy is required for the vortices to grow compared to the start-up phase at $\phi = 135°$.

3.2.3 Comparison with flat plat reduced-order model

Because the flat plat reduced-order model introduced previously (Eq. 15) only applies to an accelerating plate, it is applied to the surging airfoil between $\phi = 0°$ to 90° and between $\phi = 270°$ to 315°, where the airfoil is moving in the upstream direction. During the airfoil's motion in the downwind direction, Eq. 17 is applied for both of the motion cases, except that for $k = 0.19$ case where there are no upstream vortices, which gives zero value for $\dot{\Gamma}_{us}d_{us}$ and $\Gamma_{us}\dot{d}_{us}$. Note that the C_d values in the $\phi = 180°$ and $\phi = 225°$ cases are not calculated due to the missing information of vortex distance ($\phi = 180°$) and circulation ($\phi = 225°$), as at least one of the vortices exits the measurement domain. Also, because of missing information of vortex distance at $\phi = 180°$, the vortex separation velocity $\dot{d}$ at $\phi = 135°$ is obtained based on the backward differentiation only, contrary to the other cases where central differentiation was applied. The final result is shown in Fig. 24, where the results from the flat plate model (FP) are marked as green and yellow crosses for $k = 0.38$ and $k = 0.19$, respectively. Due to the limitation of the field of view, Eq. 17 is only applied for $\phi = 135°$ and 180°. For $\phi = 180°$, the $\dot{\Gamma}$ term in Eq. 17 is modified from the experimental result as the vortices at $\phi = 225°$ are not fully inside the FoV. Therefore, based on the portion of vortices outside the FoV as shown in Fig. 11l, a 33% ($0.2\ m^2/s$ in absolute value) increase of Γ is applied to the circulation of $\phi = 225°$. Note that the

endpoint of $\phi = 90°$ is removed from the discussion for the two motion cases as it may cause large errors in the time derivative term. The result shows a good match for the two phases of $\phi = 135°$ and 180° when the airfoil is moving downstream at $k = 0.38$. For $\phi = 135°$, $k = 0.19$ case, the flat plate model result is higher than the experiment. On the one hand, this difference is caused by the accuracy the two differential methods have, where the backward differential method used for $\phi = 135°$, $k = 0.19$ case has lower accuracy. On the other hand, by assuming zero value for $\dot{\Gamma}_{us} d_{us}$ and $\Gamma_{us} \dot{d}_{us}$, it is assumed that the downwind wake flow has no impact on the airfoil. However, even though no upwind vortices are generated, the downwind flow pushes the downwind vortices to separate. Therefore, this effect is not reflected in the model for this specific case. When the airfoil moves upstream, the FP model result matches better for $k = 0.19$ than for the $k = 0.38$ case. For the $k = 0.38$ case, the most significant error appears at $\phi = 45°$ and 90°. As shown in Fig. 2a, the airfoil decelerates at $\phi = 45°$, different from the overall accelerating trend during surging between $\phi = 0°$ and 90°. Due to this disturbance, it is speculated that the sum of the force from circulatory (Eq. 14) and non-circulatory terms (Eq. 11) cannot correctly represent the drag force. Overall, the modified model (Eq. 17) correctly reproduces the trend of the experimental results for most of the phases.

4 Conclusion

The development of vortex structures in the wake of a periodically surging NACA 0021 airfoil at 90° angles of attack has been studied experimentally at Reynolds number 1.5×10^4. The motion amplitude is fixed at 1.1 times the chord length (with peak-to-peak amplitude 2.2 times the chord length). Two motion frequencies were investigated: one with reduced frequency $k = 0.19$ and frequency ratio with respect to the static vortex shedding frequency $f/f_{st} = 0.39$; the other one with reduced frequency $k = 0.38$ and $f/f_{st} = 0.78$. Through the comparison of the two motion cases, the results focus on the vortex dynamics in a motion cycle, the total drag force, and the contributions from each component of the force.

The comparison of the two motion cases ($k = 0.19$ and $k = 0.38$) reveals significant differences in the vortex structures. For the $k = 0.38$ motion case, the vortices generate in the wake during the surging motion in the upwind direction. Conversely, at the beginning of the motion in the downwind direction, a pair of vortices start to accumulate at the upwind side. During this period, as the airfoil is moving in its own wake generated during the upwind motion, the wing's velocity is higher than the incoming flow velocity. At the end of the downwind motion, the two pairs of vortices shed simultaneously away from the airfoil. This contrasts with the $k = 0.19$ case, where the vortices are confined to the downstream side of the airfoil throughout the motion cycle. The vortices tend to be more elongated and dissipate because of turbulence.

Furthermore, this study provides clear experimental evidence of the lock-in phenomenon in both motion cases. For the $k = 0.38$ case, one pair of wake vortices and one pair of upwind vortices grow at different phases within a cycle, but shed simultaneously. For the $k = 0.19$ case, one pair of wake vortices grows and sheds within a cycle. The $k = 0.38$ case align with the result of previous work from Koopmann (1967), Anagnostopoulos (2000), and Meneghini and Bearman (1995): as the motion frequency is very close to the static shedding frequency, lock-in happens. For the latter case, the motion frequency is far from the static shedding frequency, but lock-in still happens due to the large motion amplitude. This finding aligns with and extends previous work, such as that by Choi et al. (2015), demonstrating that lock-in can happen at the sub-harmonics of the static shedding frequency, but with large amplitude.

The load estimation method was tested out on the static measurement of the airfoil, which shows fair comparison with the experimental measurement from Holst et al. (2019). Then, this method is applied to the surging airfoil to obtain the force on each phase of the motion. Both of the motion cases show that the total drag force is predominantly influenced by the mean convection force and the pressure force, and it is mainly the balance between the two that influences the trend of the total drag force. For the $k = 0.19$ case, drag is always in the same direction as the wind speed, as the wake is always occurring at the downstream side of the airfoil. For the $k = 0.38$ case, the highest drag coefficient within a cycle is around three times higher than the static case. A notable finding at this k is the occurrence of negative drag at $\phi = 135°$ where the airfoil is moving downstream. This is because at this phase, as the pressure force gives a positive contribution to the airfoil and points downstream, the mean convection force provides a larger negative deficit on the airfoil due to the preserved reversed flow in the front of the motion direction. In addition, in agreement with the result from Choi et al. (2015), the drag coefficient plot with respect to location suggests a larger force difference for the $k = 0.38$ case.

Finally, the load estimated from the experiment was compared with the reduced-order flat plate load model (Corkery et al. 2017). The original model correctly predicts the trend and fits well with the experimental data when the airfoil is moving in the upstream direction and the wake is generated in the downstream direction. The model was further refined by summing up the circulatory force from all the vortex pairs to account for the two-pair vortices condition during the downstream motion of the $k = 0.38$ case, leading to improved agreement with the experimental data.

5 Supplementary information

The supplementary material of the airfoil moving video can be found in the attached gif.

Appendix A

Uncertainty of the added mass term

To evaluate the uncertainties of the measured wing displacement, velocity and accelerations, and in turn the uncertainty of the added mass term (Eq. 9), an imposed sinusoidal curve is compared with the actual motion of the airfoil. The comparison is presented at the top of Fig. 25. Then, the motion velocity ($\dot{h}$) and acceleration ($\ddot{h}$) were calculated by analytical derivation in time. The results show very good agreement between the measured and the imposed values for both position and velocity (root mean square of the difference equal to 0.008 m and 0.37 m/s for $k = 0.38$ (0.18 m/s for $k = 0.19$), respectively). Instead, $\ddot{h}$ exhibits larger differences, especially at phases 45°, 90°, 270° and 315° at $k = 0.38$, where the uncertainty reaches maximum 57% of the measured value. Consequently, it is expected the total C_d has the largest relative difference for these cases.

The total C_d based on the theoretical added mass term obtained from the imposed h - curve is compared with the C_d where the added mass term is calculated from the actual motion. The root mean square uncertainty is calculated and is shown in Fig. 26. Overall, the added mass term on average contributes to 1.9% ($k = 0.19$) and 2.2% ($k = 0.38$) of the overall C_d. This results in a minimal change in the overall C_d value for most of the cases. On the one hand, the added mass term is inherently small due to the small wing model (small cross-section area). On the other hand, other force terms, such as the mean convection term, pressure term, etc., have a larger influence on the total C_d. Therefore, the $\ddot{h}$ calculated from the measured airfoil motion is adopted for the analysis.

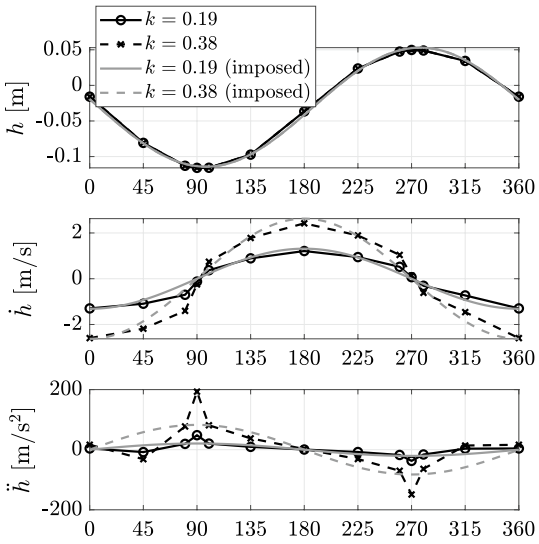

Fig. 25 Real and imposed motion (h) of the airfoil (top), and the corresponding motion velocity ($\dot{h}$) and acceleration ($\ddot{h}$)

Appendix B

C_d Non-dimensionalization issue

During the analysis, it is observed that the relative wind speed experienced by the airfoil significantly influences vortex dynamics. Therefore, in the section, the drag coefficient with the drag force (D) non-dimensionalized by the incoming wind (C_d) and the one non-dimensionalized by the relative wind (C_d^*) are compared, which is shown in Fig. 27.

The results show that when the airfoil moves upstream (between $\phi = 0°$ and 90°, and between $\phi = 270°$ and 315°), C_d^* is smaller than C_d due to a higher relative wind speed compared to the incoming wind speed. For different k cases, this difference reflects the relative effect of varying vortex dynamics. Vice versa, when the airfoil moves downstream, C_d^* is higher than C_d for both cases due to the lower relative wind speed compared to the incoming wind velocity. Additionally, when moving downstream, the influence of the relative wind speed on the vortex dynamics becomes less significant compared to that of the downwind flow velocity. Consequently, the C_d^* during this period will provide a less insightful comparison to C_d. To ensure a valid comparison

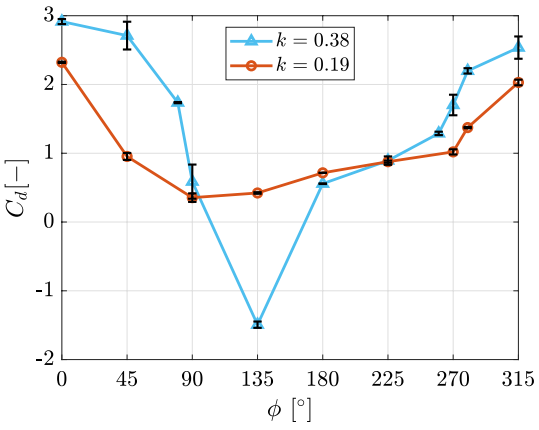

Fig. 26 Averaged total drag force coefficient C_d with the uncertainty from the added mass term marked as the black bars

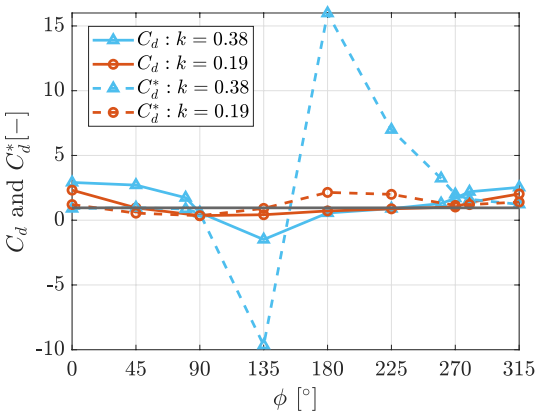

Fig. 27 Comparison between C_d $(= D/(1/2\rho U_\infty^2 c))$ and C_d^* $(= D/(1/2\rho U_\mathrm{rel}^2 c))$.The static C_d is marked as the gray horizontal line

of C_d throughout the entire surging cycle, the drag force non-dimensionalized by the incoming wind speed is used in this paper.

Supplementary Information The online version contains supplementary material available at https://doi.org/10.1007/s00348-025-04011-2.

Acknowledgements We acknowledge Sowmya Iyer for her dedicated support in the wind tunnel campaign.

Author contributions Guanqun Xu contributes to data curation, formal analysis, investigation, methodology, writing—original draft. Andrea Sciacchitano contributes to conceptualization, formal analysis, methodology, supervision and writing—review & editing. Carlos Ferreira contributes to conceptualization, formal analysis, methodology, supervision and writing—review & editing. Wei Yu contributes to conceptualization, formal analysis, funding acquisition, methodology, supervision and writing—review & editing.

Data availability The available data can be found on 4TU.ResearchData with DOI: 10.4121/0b01a240-559f-4f4b-802d-7b1d36aa0024.

Declarations

Conflict of interest The authors declare no conflict of interest.

References

Anagnostopoulos P (2000) Numerical study of the flow past a cylinder excited transversely to the incident stream. Part 1: Lock-in zone, hydrodynamic forces and wake geometry. J Fluids Struct 14:819–851. https://doi.org/10.1006/jfls.2000.0302

Bearman PW (1984) Vortex shedding from oscillating bluff bodies. Ann Rev Fluid Mech 16:195–222

Besem FM, Kamrass JD, Thomas JP, Tang D, Kielb RE (2016) Vortex-induced vibration and frequency lock-in of an airfoil at high angles of attack. J Fluids Eng, Transact ASME 10(1115/1):4031134

Bishop RED, Hassan AY (1964) The lift and drag forces on a circular cylinder oscillating in a flowing fluid. Proc R Soc Lond Ser A, Math Phys Sci 277(1368):51–75

Choi J, Colonius T, Williams DR (2015) Surging and plunging oscillations of an airfoil at low Reynolds number. J Fluid Mech 763:237–253. https://doi.org/10.1017/jfm.2014.674

Choi J, Colonius T, Williams D (2013) Dynamics and energy extraction of a surging and plunging airfoil at low Reynolds number. In: 51st AIAA Aerospace Sciences Meeting Including the New Horizons Forum and Aerospace Exposition, p 672

Corkery SJ, Stevens PRRJ, Babinsky H (2017) Low Reynolds number surge response of a flat plate wing at 90 degrees incidence. In: 55th AIAA Aerospace Sciences Meeting

Graftieaux L, Michard M, Grosjean N (2001) Combining PIV, POD and vortex identification algorithms for the study of unsteady turbulent swirling flows. Meas Sci Technol 12:1422

Heinz JC, Sørensen NN, Zahle F, Skrzypiński W (2016) Vortex-induced vibrations on a modern wind turbine blade. Wind Energy 19(11):2041–2051. https://doi.org/10.1002/WE.1967

Holst D, Balduzzi F, Bianchini A, Church B, Wegner F, Pechlivanoglou G, Ferrari L, Ferrara G, Nayeri CN, Paschereit CO (2019) Static and dynamic analysis of a NACA 0021 airfoil section at low Reynolds numbers based on experiments and computational fluid dynamics. J Eng Gas Turbines Power 141(5):51015–51016. https://doi.org/10.1115/1.4041150

Holst D, Church B, Wegner F, Pechlivanoglou G, Nayeri CN, Paschereit CO (2019) Experimental analysis of a NACA 0021 airfoil under dynamic angle of attack variation and low Reynolds numbers. J Eng Gas Turbines Power 141(3):031020. https://doi.org/10.1115/1.4041146

Lamb H (1945) Hydrodynamics. New York Dover publications

IEC (2005) 61400-1: Wind turbines part 1: Design requirements. International Electrotechnical Commission **177**

Koopmann GH (1967) The vortex wakes of vibrating cylinders at low Reynolds numbers. J Fluid Mech 28(3):501–512. https://doi.org/10.1017/S0022112067002253

Greenberg JM (1947) Airfoil in sinusoidal motion in a pulsating stream. Technical report, NACA

Meneghini JR, Bearman PW (1995) Numerical simulation of high amplitude oscillatory flow about a circular cylinder. J Fluids Struct 9(4):435–455

Morgan CE, Babinsky H, Harvey JK (2009) Vortex detection methods for use with PIV and CFD Data. 47th AIAA Aerospace Sciences Meeting including the New Horizons Forum and Aerospace Exposition, 74. https://doi.org/10.2514/6.2009-74

Van Oudheusden BW (2013) PIV-based pressure measurement. Meas Sci Technol 24:32. https://doi.org/10.1088/0957-0233/24/3/032001

Pirrung GR, Grinderslev C, Sørensen NN, Riva R (2024) Vortex-induced vibrations of wind turbines: from single blade to full rotor simulations. Renew Energy 226:960–1481. https://doi.org/10.1016/j.renene.2024.120381

Ragni D, Van Oudheusden BW, Scarano F (2011) Non-intrusive aerodynamic loads analysis of an aircraft propeller blade. Exp Fluids

51(2):361–371. https://doi.org/10.1007/S00348-011-1057-7/FIGURES/11
Rival DE, Bv Oudheusden (2017) Load-estimation techniques for unsteady incompressible flows. Exp Fluids. https://doi.org/10.1007/s00348-017-2304-3
Sarpkaya T (2004) A critical review of the intrinsic nature of vortex-induced vibrations. J Fluids Struct 19(4):389–447. https://doi.org/10.1016/j.jfluidstructs.2004.02.005
Sciacchitano A, Wieneke B (2016) PIV uncertainty propagation. Meas Sci Technol. https://doi.org/10.1088/0957-0233/27/8/084006
Sears WR (1938) A systematic presentation of the theory of thin airfoils in non-uniform motion. PhD thesis, California Institute of Technology
Shirzadeh R, Weijtjens W, Guillaume P, Devriendt C (2015) The dynamics of an offshore wind turbine in parked conditions: a comparison between simulations and measurements. Wind Energy 18(10):1685–1702. https://doi.org/10.1002/we.1781
Skrzypiński W, Gaunaa M, Sørensen N, Zahle F, Heinz J, Skrzypiński CW (2013) Vortex-induced vibrations of a DU96-W-180 airfoil at 90° angle of attack. Wind Energy 17(10):1495–1514. https://doi.org/10.1002/we.1647
Smith TR, Moehlis J, Holmes P (2005) Low-dimensional modelling of turbulence using the proper orthogonal decomposition. Nonlinear Dyn 41:275–307
Statista (2024) Cumulative installed wind power capacity worldwide from 2001 to 2023. https://www.statista.com/statistics/268363/installed-wind-power-capacity-worldwide/
Tang D, Dowell EH (2014) Experimental aerodynamic response for an oscillating airfoil in buffeting flow. AIAA J 52(6):1170–1179. https://doi.org/10.2514/1.J052077
Theodorsen T (1935) General theory of aerodynamic instability and the mechanism of flutter. Technical report, NACA
Van De Meerendonk R, Perçin M, Van Oudheusden B (2016) Three-dimensional flow and load characteristics of flexible revolving wings at low Reynolds number. Technical report x
Williamson CHK, Govardhan R (2004) Vortex-induced vibrations. Annu Rev Fluid Mech 36:413–455. https://doi.org/10.1146/annurev.fluid.36.050802.122128
Williamson CHK, Roshko A (1988) Vortex formation in the wake of an oscillating cylinder. J Fluids Struct 2:355–381
Xu G, Yu W, Ferreira C, Sciacchitano A, Iyer S (2024) Experimental comparison of a NACA0021 airfoil in large plunging and surging motions at 90° angle of attack. J Phys: Conf Ser 2767(2):022047. https://doi.org/10.1088/1742-6596/2767/2/022047
Xu G, Yu W, Sciacchitano A, Ferreira C (2025) An experimental study of the unsteady aerodynamics of a static DU91-W2-150 airfoil at large angles of attack. Wind Energy. https://doi.org/10.1002/we.2974
Ye Q, Schrijer FFJ, Scarano F (2016) Boundary layer transition mechanisms behind a micro-ramp. J Fluid Mech 793:132–161. https://doi.org/10.1017/JFM.2016.120
Young J, Lai JCS (2004) Oscillation frequency and amplitude effects on the wake of a plunging airfoil. AIAA J 10(2514/1):5070
Young J, Lai JCS (2007) Vortex lock-in phenomenon in the wake of a plunging airfoil. AIAA J 10(2514/1):23594